Experimental Thermal and Fluid Science 97 (2018) 484–501

Contents lists available at ScienceDirect

Experimental Thermal and Fluid Science

journal homepage: www.elsevier.com/locate/etfs

Comparison of disturbance wave parameters with flow orientation in vertical annular gas-liquid flows in a small pipe

Joao Vasques[a], Andrey Cherdantsev[b,c], Mikhail Cherdantsev[b], Sergey Isaenkov[b], David Hann[a,*]

[a] Faculty of Engineering, University of Nottingham, Nottingham, United Kingdom
[b] Kutateladze Institute of Thermophysics, Novosibirsk, Russia
[c] Novosibirsk State University, Novosibirsk, Russia

ARTICLE INFO

Keywords:
Annular flow
Disturbance waves
Ripple waves
Flow orientation
BBLIF technique

ABSTRACT

The interfacial wave structure of the liquid film in both upward and downward annular gas-liquid flows in an 11.7 mm pipe were investigated using the Brightness Based Laser Induced Fluorescence technique (BBLIF). Film thickness measurements were carried out with high spatial and temporal resolution between 330 and 430 mm from the inlet, where the properties of disturbance waves are almost stabilised. Using a tracking algorithm to detect disturbance waves, a full characterisation in terms of their velocity, frequency, longitudinal size and spacing was carried out. Direct comparison between both flow orientations while testing the same flow conditions shows that although the flow orientation does not affect the velocity of disturbance waves, the fraction of film surface occupied by the disturbance waves is smaller in upwards flow. Thus, more liquid travels in the base film in upwards flow, which is consistent with the base film thickness measurements. These observations, together with qualitatively different behaviour of ripple wave velocity in upwards and downwards flows, studied using 2D Fourier analysis, indicate that the role of gravity is much more important on the base film than on disturbance waves. This supposedly occurs due to a local decrease in the interfacial shear stress on the base film surface because of the resistance of the disturbance waves to the gas stream in upward flow.

1. Introduction

In two-phase gas-liquid flows, different flow regimes can be encountered depending on input parameters such as the flowrates and the properties of both phases, the dimensions of the duct and on the orientation of the flow. The regime of interest in this paper is the annular flow regime, which generally is observed at high gas flowrates and encountered in a wide range of industrial applications, such as transfer pipelines and risers present in the oil-and-gas industry; condensers and evaporators encountered in nuclear reactors and chemical reactors encountered in chemical processing plants [1]. In this regime, the liquid travels in the form of a thin and wavy film in contact with the walls of the duct, while being sheared by a co-current high-velocity gas stream that occupies the core of the duct. Additionally, liquid droplets can be found in the gas core due to entrainment of the liquid film, while gas bubbles can be entrained into the liquid film.

One very important feature of annular flows is the presence of thick, fast-moving interfacial structures, best known as ‘disturbance waves’ (also referred to as ‘roll’ waves in literature). These structures travel over a thin residual liquid layer, often referred to as ‘base film’. Additionally, the disturbance waves are generally characterised as having an amplitude several times higher than the mean thickness of the liquid film, by being coherent around the circumference of small-diameter pipes and by moving with large and approximately constant velocity over long downstream distances [2]. These sets of conditions presume that the flow has achieved a developed state, which takes considerable distances from the inlet for stabilisation to occur. Prior to stabilisation, the disturbance waves undergo a downstream decrease in frequency due to coalescence [3], complex behaviour of velocity [4] and gradual downstream increase in transverse coherence [5]. There is conflicting evidence on the exact length required for stabilisation of their properties [4]. The surface of both the disturbance waves and the base film between them is covered with numerous short-lived small-scale structures, commonly known as ‘ripple’ waves.

The disturbance waves are objects of complex structure and are still of an unclear nature. It is not even obvious that the word “waves” is applicable to them. They generate small-scale waves – the ripples – on their rear slopes [6]. Ripples generated far enough from the front of a disturbance wave lag behind it and travel with low velocity until the following disturbance wave overtakes them. Ripples generated closer to

* Corresponding author.
E-mail address: David.Hann@nottingham.ac.uk (D. Hann).

https://doi.org/10.1016/j.expthermflusci.2018.03.020
Received 18 October 2017; Received in revised form 10 March 2018; Accepted 19 March 2018
Available online 29 March 2018

Nomenclature

A	amplitude [m]
b	cross-correlation function [m^2 s]
c	phase velocity from ω–k analysis [m/s]
C	compensation matrix [–]
D	pipe diameter [m]
f	frequency [Hz]
g	acceleration due to gravity [m/s^2]
h	film thickness [m]
Int	intermittency [–]
J	intensity of light recorded [a.u.]
k	wave number [rad/m]
K	reflection index [–]
L	wave spacing [m]
L_{DW}	longitudinal size [m]
N	number of samples [–]
Q	volumetric flowrate [m^3/s]
q	volumetric flowrate per unit width [m^2/s]
Re	Reynolds number [–]
s_m	standard mean error [%]
t	time [s]
T	time separation between waves [s]
T_{DW}	temporal length of wave [s]
V	velocity [m/s]
x	longitudinal coordinate [m]

Greek letters

α	absorption coefficient [1/m]
Δ	delta, shift [–]
λ	wavelength [m]
μ	dynamic viscosity [kg/ms]
ν	kinematic viscosity [m^2/s]
ρ	density [kg/m^3]
σ	standard deviation [–]
τ	time delay [s]
τ_s	interfacial shear stress [Pa]
ω	angular frequency [rads/s]

Subscripts

0	reference signal
b	base
c	cross-correlation
G	gas
L	liquid
N	normalised
max	maximum
min	minimum
RW	ripple wave
S	superficial
DW	disturbance wave
$\langle\rangle$	averaging of value

the front move faster than the disturbance wave and can be torn into droplets by the gas stream. The ability to generate the fast ripples is a distinctive feature of the disturbance waves, which might indicate the existence of an eddy motion under the humps of disturbance waves [6–7].

The prediction of the behaviour of disturbance waves is of significant importance for researchers due to their dominant role in the heat and mass transfer characteristics of the annular flow regime [5,8]. More specifically, the presence of disturbance waves influence the shear stress at the gas-liquid interface, together with the wall shear stress underneath them. Moreover, it has been established that liquid entrainment into the gas core is linked to the presence of the disturbance waves. These factors ultimately have an impact on the overall pressure drop across the system. Furthermore, it has been found that heat transfer rates are enhanced in the areas where disturbance waves are present, whereas the laminar regions in between consecutive disturbance waves display much lower heat transfer values [9]. As a result, the study of annular flows in a variety of configurations has been conducted in an attempt to improve the understanding of such types of flows and to advise the different industries about integral characteristics such as pumping requirements, the fraction of liquid that is entrained, or the onset of flooding conditions. The achievements are still far from proper generalisations due to the mostly empirical character of the research and the huge number of flow parameters which vary in different experiments and affect the properties of the disturbance waves and integral flow characteristics. Such flow parameters include the physical properties of both liquid and gaseous phases; size and shape of the duct; flow orientation; distance from the inlet; presence of heat flux, phase transitions, chemical reactions, etc.

In the present study we would like to focus on the effect of flow orientation, or, to be precise, on direct comparison between upward and downward annular flows in a vertical circular pipe. It would be useful to analyse the influence of the angle between the flow and the gravity on the properties of the disturbance waves for the two extreme cases *ceteris paribus*. One particular practical motivation of such a study is related to pipelines with vertical return bends where the two cases may occur simultaneously in different parts of the duct.

Comparisons of this kind have previously mostly been made in different regimes of gas-liquid flows at relatively low gas superficial velocities. The effect of flow orientation on transitions between flow patterns has been conducted by Bhagwat and Ghajar [10], Jiang and Rezkallah [11], Lee et al. [12], and Oshinowo and Charles [13]. These studies found that the correlations for transitions developed in upward flows do not work properly in the downward case. Besides, different flow patterns at the transition to annular flow were observed: in the downward flow a decrease in the gas velocity leads to a falling-film flow instead of the churn flow pattern typically found in upward flow. The average void fraction was found to be noticeably higher for downward flow, but the difference decreases with increasing gas flow rates, becoming very small when annular flow pattern is achieved. In their analysis of the transition to liquid entrainment Ishii and Grolmes [14] considered upward, downward and horizontal flows. Their theory predicts that the transition to entrainment occurs at the same conditions in upward and horizontal flows but, in a certain range of liquid flow rates, it can occur at lower gas velocities in downward flow.

Particular studies have been devoted to the comparison of integral characteristics of annular flow. Wallis [15] compared the fraction of liquid travelling as droplets (so-called “entrained fraction”) in upward and downward annular flows, see also [16]. Similar values of this quantity have been measured at high gas velocities, far enough from the churn flow conditions. At low liquid flow rates, the entrained fraction was seen to be slightly higher in upward flow, but the difference decreased even further at larger liquid flow rates. Hughmark [17] reported data analysis on pressure drop and heat transfer measurements in annular flow with phase change with upward, downward and horizontal flow orientation. Reasonable applicability of the correlations developed for the upward flow to horizontal and downward flows was found, though the error was large in all the cases. Antipin et al. [18] conducted measurements of time-averaged film thickness and pressure gradient in upward and downward orientations of the same pipe at the same flow parameters. Both quantities were shown to be slightly higher in the upward configuration, though the difference decreased with

increasing gas velocity.

Recently, Anupriya and Jayanti [19] presented a study on the comparison of film thickness and pressure drop in upward and downward annular flow. It was concluded that the correlations for pressure drop developed in upward flows do not properly describe downward flow.

To the best of our knowledge, no systematic direct comparison of the properties of disturbance waves in upward and downward annular flows was previously conducted. At the same time, numerous measurements were made separately for upward annular flow [2,4–5,20–30] and for downward annular flow [1,31–34]. This list is far from complete; still, it can be noticed that the upward flow has received more attention.

The majority of these studies ignore the complexity of the disturbance waves described above, regarding the disturbance waves as solitary surface waves like those in the ocean or on falling liquid films. In such an approach the disturbance waves can be described by a number of quantities such as ***amplitude***, A, propagation ***velocity***, V, and passing ***frequency***, f. As a rule, these properties were measured by analysing temporal records of film thickness obtained by conductivity probes at fixed locations. The average velocity of the disturbance waves was usually determined based on cross-correlation shift between two records obtained by a pair of adjacent probes. The passing frequency was most often estimated as the frequency of maximum power in the power spectrum of the record. To obtain the amplitude of the waves, the local maxima in a record were found and, after filtration of the maxima of the ripples, film thickness values in those points were averaged. In simplified cases, the amplitude of disturbance waves was estimated as the standard deviation of the film thickness record. Disturbance waves ***spacing***, L, is also important since the passing frequency is strongly related to the velocity. Spacing is defined as an average distance between adjacent disturbance waves, and is usually calculated as ratio of velocity to frequency. Sometimes it is erroneously referred to as "*wavelength*", though the latter implicitly assumes the regular character of the waves. In the case of irregular – or solitary – structures such as the disturbance waves there is no direct relation between the ***longitudinal size***, L_{DW}, of a disturbance wave and the distance between adjacent disturbance waves. The ratio of average size to average spacing – i.e., the fraction of film surface occupied by disturbance waves – is referred to as ***intermittency***, *Int.* As a rule, this quantity is defined in the temporal domain, as the ratio of the average duration of passage of a disturbance wave over particular coordinate (which could be called "*temporal length*", T_{DW}) to the average time period between arrivals of two adjacent disturbance waves (this is often called "*time separation*", T). The average time separation is usually calculated as a reciprocal to the passing frequency, and the longitudinal size of a wave is a product of its temporal length by its velocity. Thus, the intermittency can be estimated as

$$Int = \frac{\langle T_{Dw} \rangle}{\langle T \rangle} = \frac{\langle L_{Dw} \rangle f}{\langle V \rangle} = \frac{\langle L_{Dw} \rangle}{\langle L \rangle} \tag{1}$$

A number of the qualitative dependencies of disturbance waves properties on gas and liquid flow rates obtained in these studies are valid for both flow orientations. In particular, speed and frequency of the disturbance waves grow linearly with increasing gas superficial velocity and – in less pronounced and less linear manner - with increasing liquid flow rate. This regularity is observed in almost all of the aforementioned studies. The amplitudes of disturbance waves grow with liquid flow rate [1] but decrease with increasing gas velocity [23]. The thickness of the base film over which the disturbance waves propagate behaves in the same manner as the amplitude of the waves' and mean film thickness [23,33]. The spacing was found to decrease with both gas and liquid flow rates [20], reaching saturation at high enough liquid flow rates [22,25].

The results on the intermittency are quite contradictory. In some cases the intermittency is calculated in integral manner as fraction of time when film thickness is higher than certain threshold [32]. The other way is to directly measure either temporal or spatial longitudinal size of each disturbance wave individually [29]. Schubring et al. [28] showed that different methods yield significantly different results. In general it could be stated that intermittency is usually varied in the range between 0.1 and 0.4 and that it mainly grows with liquid flow rate, while the dependence on gas velocity is weak. The longitudinal size of the disturbance waves can also be determined in different ways. Alekseenko et al. [31] distinguished the length of the crest of a disturbance wave covered with fast ripples, length of a disturbance wave's rear slope and the length of stabilisation of properties of slow ripples generated by the disturbance wave. In other papers [1,21,28], a simpler idea of film thickness threshold was used to detect the beginning and the end of a disturbance wave. Generally, the longitudinal size weakly grows with liquid flow rate and weakly decreases with gas velocity.

A quantitative study of the effect of flow orientation on the properties of disturbance waves using only the literature data would be complicated due to varying conditions – such as ranges of phases flow rates, pipe diameters, distance from the inlet, system pressure and physical properties of the phases – in the works of different authors. To conduct such a study, a new cycle of experiments was performed in both upwards and downwards annular flow situations in the same pipe, at the same distance from the inlet, with the same gas and liquid flow rates. In order to provide a higher level of characterisation of the disturbance waves, spatiotemporally resolved film thickness measurements were conducted using the brightness based laser induced fluorescence technique (BBLIF). This approach will also help to test the validity of different averaging techniques. The results will be useful in the improvement of existing semi-analytical models, and to provide validation data for potential computational fluids dynamics (CFD) simulations that aim to predict such flows.

2. Experimental apparatus and procedure

2.1. Experimental setup

In this work, both upwards and downwards adiabatic air-water annular flows were studied in an acrylic resin pipe with an internal diameter $D = 11.7$ mm. For direct comparison on the effects of flow orientation, the same flow parameters were tested for both experiments, with the Reynolds number, Re_L, for the liquid varying from 140 to 400. Here, Re_L is defined based on the liquid flowrate, Q_L, the kinematic viscosity, ν, and the pipe perimeter, πD, thus being four times smaller than the liquid Reynolds number constructed using the liquid superficial velocity, V_{SL}, as shown in Eq. (2):

$$Re_L = \frac{Q_L}{\pi D \nu} = \frac{V_{SL} \pi D^2}{4 \pi D \nu} = \frac{V_{SL} D}{4\nu} \tag{2}$$

To measure the liquid flowrate, a rotameter was employed. For its calibration, a measuring cylinder was filled with water for 100 s at different flowrates. Consequently, the error associated with its calibration was measured to be 1.4%. By combining the error associated with taking readings from the rotameter, the total uncertainty associated with the liquid flowrate measurement was calculated to be 2%.

The range of superficial gas velocities tested, V_G, was 22–57 m/s, and was calculated as follows:

$$V_G = \frac{4 Q_G}{\pi D^2} \tag{3}$$

The gas flowrate, Q_G, used in Eq. (3), was measured using a U-manometer, which compared the pressure difference between sensors before and after an orifice plate. The calibration of the U-manometer was achieved with a rotational air flowmeter RVG (Elster GmbH). The calibration curve was obtained over the flow range of $Q_{min} = 3\ m^3/h$ up to $Q_{max} = 100\ m^3/h$. Consequently, the relative error on the flowrate measured ranged from 1% to 2% over the following intervals:

$$\pm 2\% \ at \ Q = Q_{min}{-}0.1Q_{max} \quad (4)$$

$$\pm 1\% \ at \ Q = 0.1Q_{max}{-}Q_{max} \quad (5)$$

By combining with the error associated with reading the manometer, the total uncertainty associated with the gas flowrate measurement ranged from 1.5 to 2.5% depending on the gas flowrate interval being measured.

In order to perform the experimental campaign, the following setup was employed, as seen in Fig. 1(a).

Compressed air from the mains is first introduced into the test section through a concentric metal tube with an internal diameter of 10.1 mm and wall thickness of 0.3 mm. Before starting the experimental campaign, water was pumped into the header tank placed 2.5 m above the inlet. The pump was then switched off and water flowed under gravity. The water entered the test section through the manifold, which consists of a 0.5 mm ring slot between both the test section and the concentric metal pipe. This manifold ensured that annular flow started directly from the inlet. This multiphase mixture travelled through the test section before exiting into a cyclone separator. The air was discharged to the atmosphere and the liquid was returned to the header tank. In order to test annular flow conditions in an upwards configuration, both the testing and mixing section were rotated 180° and the same procedure described above was repeated.

If water at room temperature is sheared by a high-velocity gas stream, it undergoes evaporation, which results in a decrease of the liquid temperature. After 1–2 h of running the rig in working conditions, an equilibrium temperature of 16 °C was reached, which corresponds to a liquid kinematic viscosity, ν, of 1.15×10^{-6} m^2/s. During the experiments, the temperature and total volume of the water were controlled to ensure that no significant evaporation took place. Such a precaution allowed us to stay within the purely hydrodynamic problem statement.

2.2. Measurement technique

This study will report on the film thickness measurements conducted using BBLIF technique at axial distances that range between 330 and 430 mm (between 28 and 37D) from the inlet in both upwards and downwards flow configurations. Although fully developed annular flow has not been achieved at this stage, results show that this is close to being achieved, and nonetheless, direct comparison of different flow parameters can be achieved at the same axial locations for both flow orientations.

The BBLIF technique is a diagnostic tool that is based on the dependence of local intensity of excited fluorescence light on the local thickness of the liquid layer. The advantages of employing this technique are:

- Non-intrusive technique, therefore, it does not affect the flow behaviour;
- Field measurements of local film thickness can be resolved in both longitudinal and transverse coordinates and in time, though, in the present experiments, the measurements were resolved only in longitudinal coordinate, x, and time, t;
- High spatial resolution: limited mostly by the optical configuration;
- High sampling frequency: limited mostly by the equipment capabilities;
- It is possible to study droplets in the gas core and bubbles entrained in the liquid film simultaneously with waves of various types.

Fluorescent dye, dissolved in the liquid, is excited by an external light source whose wavelength matches the absorption wavelength of the fluorescent dye. Upon excitation, the fluorescent dye present in the liquid phase absorbs the light energy and re-emits it at a different wavelength that can be recorded by a high speed camera equipped with a low-pass optical filter to prevent registration of reflected/scattered laser light. The local intensity of the fluorescent light, $J(x,t)$, is exponentially related to the local film thickness, $h(x,t)$, given by the following relationship:

$$J(x,t) = C(x,t)\cdot[1{-}\exp(-\alpha h(x,t))]\cdot[1 + K\cdot\exp(-\alpha h(x,t))] + D(x) \quad (6)$$

where α is the absorption coefficient of fluorescent light; K is the reflection index at the liquid-gas interface (equal to 2%); $C(x)$ is the compensation matrix, used to compensate for spatial non-uniformity of excitation light; $D(x)$ is the dark level of the camera. All these quantities are defined either in auxiliary experiments or during the calibration procedure for each experimental run. Details on how α was estimated can be found in Alekseenko et al. [35]. The method to estimate the compensation matrix, $C(x0)$, involves obtaining the time-averaged brightness of fluorescence, $J_0(x)$, emitted by a reference flow whose time-averaged film thickness, $h_0(x)$ is known in the section of the pipe where film thickness measurements are to be obtained. Eq. (7) is then re-arranged in order to obtain the only unknown, $C(x)$. In this experimental campaign, different ways to organise reference signals

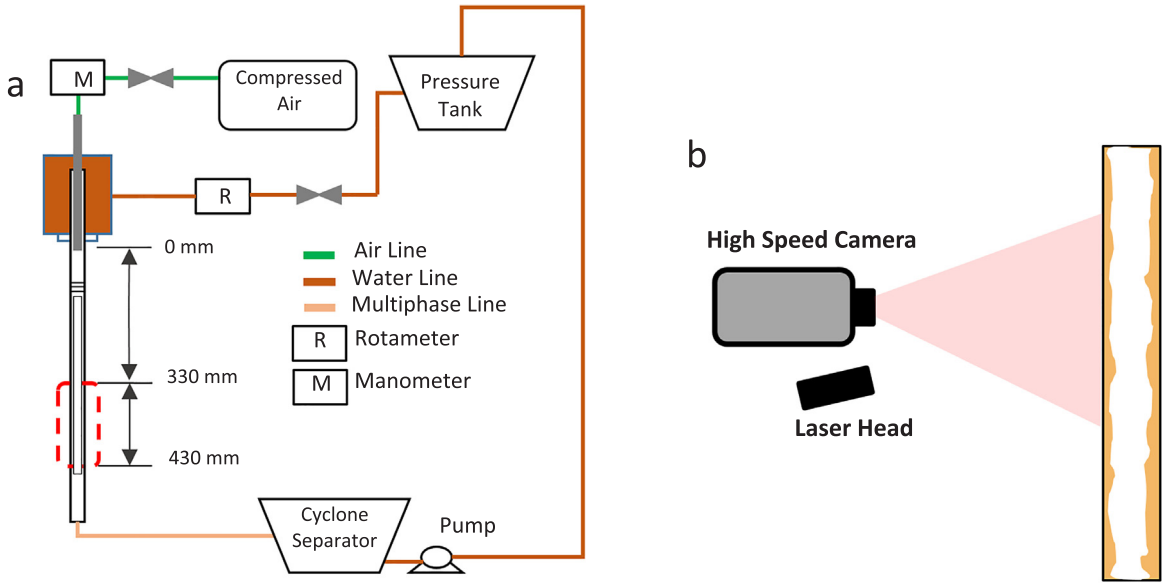

Fig. 1. (a) Diagram of experimental set-up; (b) Implementation of the BBLIF technique.

were used for downward and upward flow scenarios. For the downwards flow, a configuration where a thin liquid film with $Re_L = 40$ flowing under gravitational action in the absence of gas flow (so-called 'falling film flow') was present. In this case, the average film thickness is well described by the Nusselt solution of the Navier-Stokes equations for flows with a laminar waveless liquid film. For the upwards flow, it is impossible to organise such a configuration. Still, the reference matrix is necessary, since it cannot be guaranteed that the local illumination remains the same after turning the working section upside down and re-adjusting the optical system. To create a reference signal in such a case, it was assumed that the flow of a very thin liquid film under very strong gas shearing action is insensitive to the flow orientation. This assumption is supported by observations of Alekseenko et al. [36], who studied the spectral structure of thin gas-sheared liquid films in downward annular flow without entrainment. They have noticed that for high enough V_G the power spectra of film thickness records showed strong similarity at very different gas velocities. The deviations from the observed universal shape were detected at low gas velocities and were attributed to the influence of gravity. The region of self-similarity for water starts at $V_G > 27$ m/s. Thus, the flow of a thin liquid film with $Re_L = 40$ and $V_G = 36$ m/s was used as a reference signal to obtain $J_0(x)$ for the upward flow. The values of were taken from the BBLIF-measurements conducted in downward flow for the same Re_L and V_G.

As discussed by Alekseenko et al. [35], the performance of Eq. (7) was checked by measuring the fluorescent light intensity in slots of different thickness with the working fluid. The different slots depths were created by coaxially inserting blackened rods of different diameter which created predetermined depths of known thickness between the pipe wall and the rods. in this case was considered to be zero. These experiments have confirmed the validity of Eq. (7), as deviations did not exceed the tolerance of the inner diameter of the blackened rods.

Alekseenko et al. [31] estimated that the overall error of the film thickness measurement in the base film and at the rear slope of disturbance waves as 5–6%. This is composed of a 2–3% error due to camera noise, in addition to another 2–3% error caused by non-uniformity of individual pixels after the compensation procedure. At the crest of a disturbance wave, where fast ripples are present, the error can increase significantly due to internal reflection of the laser light under a high-slope of gas-liquid interface. This yields in non-physical film thickness values. However, the effect of optical distortion can be reduced and minimised by means of thresholding, thus allowing to easily identify and remove these non-physical values from consideration.

In order to implement the BBLIF technique, rhodamine 6G was added to water at a concentration of 15 mg/l. A continuous 3 W laser with a wavelength of 532 nm was used. A high-speed Photron FASTCAM SA5 camera equipped with a 550 nm cut-off wavelength orange filter was used to record the fluorescent light reemitted by the dye upon being excited by the laser light, as shown in Fig. 1(b). The temporal resolution was 10 kHz, with 1 and 2 s records obtained for each flowrate combination of the upwards and downwards configurations, respectively. For both experiments, this study will report on the results obtained by analysing the local film thickness in a two-dimensional approach, where the camera was focused at the central portion of the test section. The spatial resolution of the acquired images ranged from 0.1 to 0.45 mm/pixel for upwards and downwards flow experiments respectively (with a 1×1024 pixels matrix for upwards flow and 1×220 pixels for downwards flow). The images were recorded in 8-bit format, thus meaning that there are 256 levels on intensity that can be recorded per each pixel. The average amplitude of the waves (and therefore, the maximum brightness of emitted fluorescent light) depends on the flow parameters being tested. Consequently, in order to achieve an optimum correspondence between the brightness of the fluorescent light and the dynamic range of the camera, the exposure time was varied between 5 and 10 μs. Upon acquiring the images and re-constructing them into film thickness information, the re-constructed information for each axial slice at each particular time was stacked together, resulting in a spatiotemporal plot of the film thickness, $h(x,t)$.

3. Data processing and results

3.1. Spatiotemporal data and structure of results

Fig. 2 shows examples of spatiotemporal records of the film thickness, obtained at 330–430 mm from the inlet. Short fragments of the full records obtained are shown here, where the flow direction is from left to right in both images. The spatiotemporal plots are therefore a visual display of temporal evolution of the film thickness over a range of axial locations.

Many qualitative events can be obtained from the observation of such spatiotemporal plots, which aid researchers to better understand and characterize the behaviour of disturbance and ripple waves in a close to developed condition. This has been extensively detailed in the work of Alekseenko et al. [6,31,35], which serve as the backbone of this annular flow study.

The local brightness of the spatiotemporal plots is directly proportional to the value of film thickness. The bright 'stripes' seen in Fig. 2

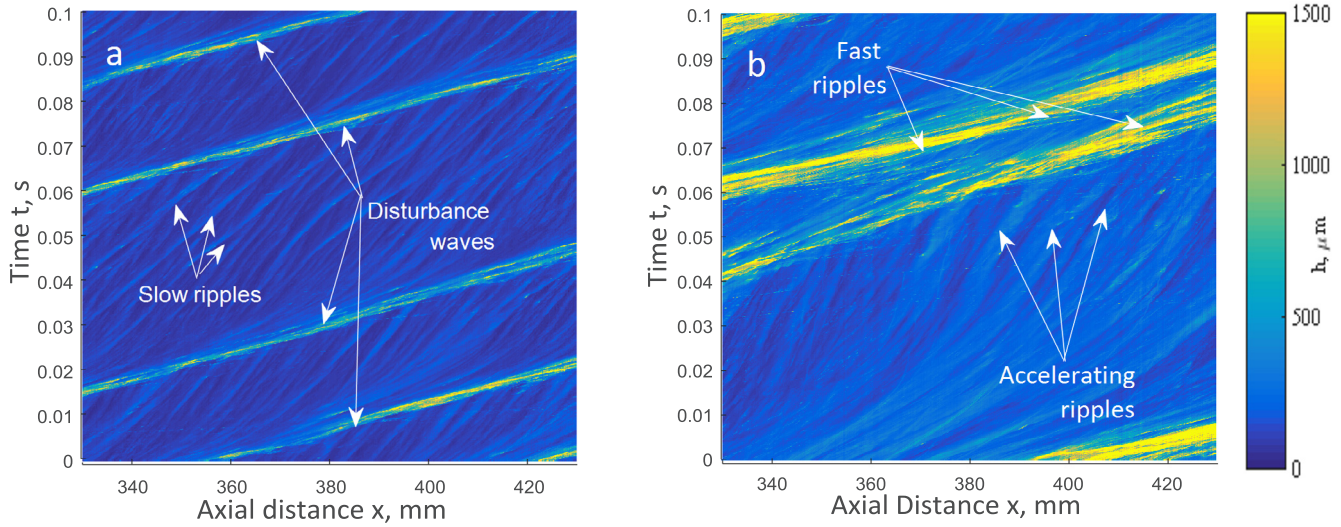

Fig. 2. Example of spatiotemporal records of film thickness obtained for upwards annular flow at $Re_L = 400$ for gas flowrates: (a) $V_G = 36$ m/s; (b) $V_G = 22$ m/s. Important features that have been studied in previous works are identified for discussion in the text.

correspond to the spatiotemporal trajectories of disturbance waves, where it can be observed that their height is several times larger than the thickness of the base film between them. The velocity of the waves is proportional to the angle between the spatiotemporal trajectories and the -axis. The disturbance waves are seen to have their individual velocity, which in certain cases leads to the coalescence of consecutive disturbance waves, where the resultant wave possesses the velocity of the faster former individual wave.

The base film is seen to be covered with ripples with velocity much lower than that of the disturbance waves. These ripples are seen to be generated at the rear slopes of the disturbance waves, where they typically slide back to the base film behind the parent disturbance wave and travel at a relatively constant velocity until the following disturbance wave absorbs them. Close to this stage, the ripple wave can accelerate at a certain rate. However, depending on the relative position of origin, the 'new born' ripples can also travel faster than the parent disturbance waves, travelling towards the front of the disturbance wave crest and disappearing there. This is due to the disruption of the fast ripple by the gas shear into droplets through either bag or ligament break-up mechanisms.

Finally, it can be seen that the disturbance wave trajectory is close to linear, thus meaning that they are travelling at a constant velocity, which is one of the pre-requisites to satisfy the fully developed condition. This is going to be discussed in more detail in Section 3.2. It is worth mentioning that the disturbance waves exhibit a high level of non-periodicity.

An important feature of such plots is that it allows not only for qualitative observations, but also for quantitative analysis to be made, where its information can be processed in a variety of ways. One approach that can be taken, is to analyse each temporal record of film thickness for each axial location individually, similarly to what has been done in the past using pointwise measurements techniques such as conductance probes, but this time, with a much larger number of 'probes' (i.e. camera pixels). Using this interpretation, different parameters can be measured. These include mean and average base film thickness, wave velocity by means of cross-correlation, and wave frequency by spectral analysis. These methods will be herein described as *indirect methods*, since the whole temporal plot is processed at once, and its properties are assumed to be related to the disturbance wave behaviour. These will be described in more detail through Section 3.2, where the effect that downstream distance has on the flow development is also considered. In Section 3.3, the approach employed to automatically track each individual disturbance wave present in the spatiotemporal plots is described. This can be seen as a *direct method* to measure the different aforementioned parameters. The performance of the *direct* versus *indirect* approaches is also reported here. Based on the best procedures to analyse the disturbance wave behaviour, a direct comparison of the effect of flow orientation on the annular flow regime is made in Section 3.4. This is extended to the study of the motion of the slow ripples located in the base film between consecutive disturbance waves, which is covered in Section 3.5. Finally, Section 4 provides a conclusion of the main findings of this study.

3.2. Indirectly measured parameters and effect of downstream distance

3.2.1. Thresholding procedure to calculate base and mean film thickness

As discussed in Section 2 an overestimation of the true film thickness can occur at the crests of disturbance waves with BBLIF due to total internal reflection of the laser light when incident to a large gradient at the gas-liquid interface. This results in an error in the film thickness measurement that surpasses the 5–6% estimated film thickness error that can be encountered in the base film and the back slope of the disturbance waves. To reduce the effect of optical distortions on the film thickness measurements, values of film thickness above 1.5 mm were cut-off by that level for both upwards and downwards configurations.

Fig. 3 shows an example of a time series record for a single axial location for the case of $Re_L = 400$ and $V_G = 22$ m/s in upwards flow, where the implementation of the thresholding procedure can be seen.

The mean value of film thickness was obtained for each individual axial location of the spatiotemporal plots. To measure the base film thickness, the same procedure was repeated, where only the points below the mean film thickness were taken into consideration. To estimate the effect of downstream distance, a linear approximation of the dependence of a quantity on x was calculated, and the values of this approximation at the borders of the region on interrogation ($x_1 = 330$ mm and $x_2 = 430$ mm) were plotted against one another, as shown in Fig. 4. The variation of both mean and base film thickness with downstream distance is generally within 10% deviation. The error bars in Fig. 4 were obtained based on the standard deviation of the $\langle h \rangle(x)$ and $h_b(x)$ arrays.

This is a first indication that the flow is close to a fully developed state. To obtain the average mean and base film thicknesses for a regime point, the average value of the whole $h(x,t)$ was calculated. These will be discussed in more detail in Section 3.3.

3.2.2. Application of cross-correlation function for indirect disturbance wave velocity estimation

To estimate the average velocity of the waves at point x, the cross-correlation function of a pair of temporal records, $h(t,x_1)$ and $h(t,x_2)$, where $x_1 = x-\Delta x$ and $x_2 = x + \Delta x$, was calculated as function of time delay, τ:

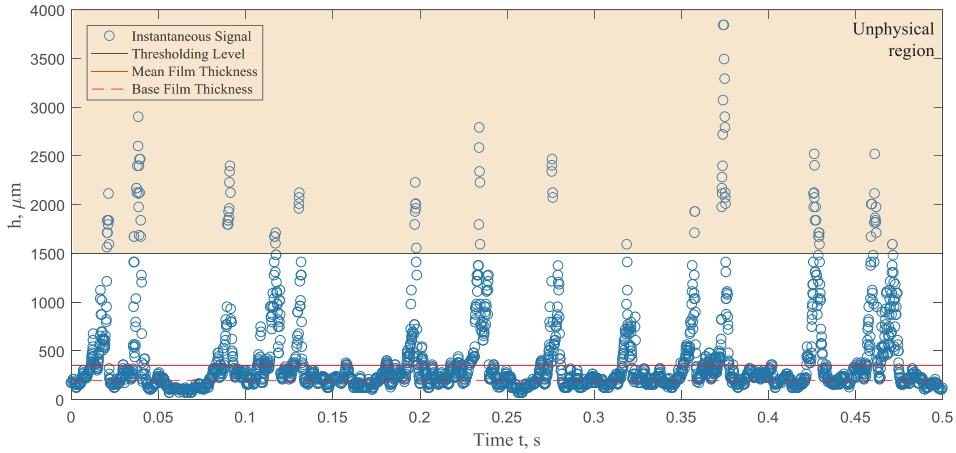

Fig. 3. Example of the thresholding of the instantaneous film thickness being applied to overcome overestimation of the film thickness due to total internal reflection of laser light under high-slopes of the gas–liquid interface. This example refers to $Re_L = 400$,$V_G = 22$ m/s in upwards flow.

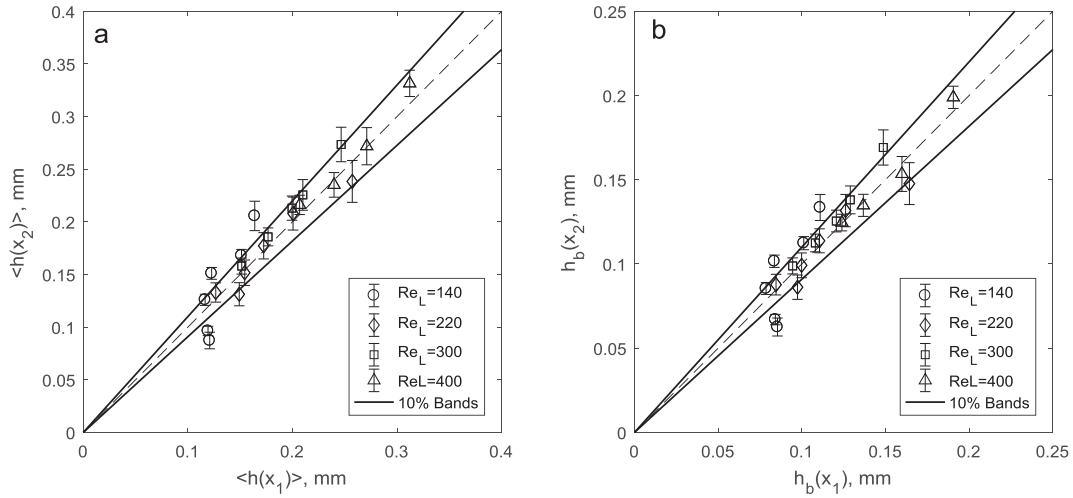

Fig. 4. Evolution of (a) mean and (b) base film thickness between $x_1 = 330$ mm and $x_2 = 430$ mm for the upwards configuration. The error bars displayed were obtained by measuring the root-mean-square error of the linear approximation for each data point. V_G varies between 22 and 57 m/s.

$$b(x_1,x_2,\tau) = \sum_t (h(t,x_1)-\langle h(t,x_1)\rangle)(h(t+\tau,x_2)-\langle h(t+\tau,x_2)\rangle) \quad (7)$$

The parameter τ is varied in a wide range of both positive and negative values with step equal to the sampling period. The value of τ at which the correlation reaches its maximum value, characterises the time shift between the two records. The value of Δx was selected to ensure reasonable trade-off between spatial localisation of the measurements and the accuracy of the time shift measurements. In order to improve the latter, a parabolic interpolation of the vicinity of the maximum of the $b(\tau)$-function was obtained and the value of τ corresponding to the maximum of the fitted parabola (τ_{max}) was taken as the time shift estimation. The local average velocity, $V_c(x)$ is then defined as $2\Delta x/\tau_{max}$. Since the disturbance waves are of high amplitude, their contribution into the cross-correlation function is expected to be the most significant and thus the time shift between the temporal records is expected to correspond to the velocity of the disturbance waves.

Observation of the evolution of disturbance wave velocity, as seen in Fig. 5, shows only a slight but systematic increase in wave velocity with axial distance (around 5% increase). Therefore, this represents that the waves are close to reach a fully developed state, since their velocity is almost constant. The error bars were obtained in the same manner as those in Fig. 4. To obtain the average velocity for a regime point, $\langle V\rangle$, the average value of $V_c(x)$ was calculated.

3.2.3. Application of Fast Fourier Transform (FFT) function for indirect disturbance wave frequency estimation

A commonly used *indirect method* to estimate the wave frequency is to determine frequency of maximum power in the power spectral density (PSD) of a temporal record of film thickness. The PSD is obtained from the average of the results using the *Welch* algorithm [37] with zero overlap between the 5 equal segments of a particular film thickness time series at each spatial location measured. The spectra are smoothed to further decrease noise using a 7 point running average filter.

Fig. 6 shows an example of 4 PSD cases obtained for various gas and liquid flowrate combinations. The flow is close to a fully developed state, so the variation of the maximum power in the PSD plots with axial location is weakly pronounced, although there is still some level of coalescence between neighbouring disturbance waves. Consequently, in order to calculate the mean passing frequency of disturbance waves f_{max}, an average frequency of the maximum power obtained for each axial location across the entire PSD plot was obtained for all the regime points. The uncertainty associated with the application of the FFT is a function of the uncertainty on the PSD result (magnitude) and the error of the time step of the frequency measurement. The former is reduced $\sqrt{N}$ times due to the averaging [37], where N is the number of samples used in the frequency measurement, while the frequency step is 5 and 2.5 Hz for the upward and downward cases respectively. The implications of such a high level of uncertainty will be discussed in greater detail in Section 3.3.2.

3.3. Directly measured disturbance wave parameters obtained using tracking algorithm

In the previous section, the *indirect* methods typically employed in the studies of the disturbance wave behaviour were covered. These have been classically employed in the multiphase flow field mainly due to the constraints of the measurement techniques available for the study of such flows. As shall be seen later, the uncertainty associated with such methods can be significant, thus affecting the interpretation of the disturbance wave behaviour. However, through the construction of

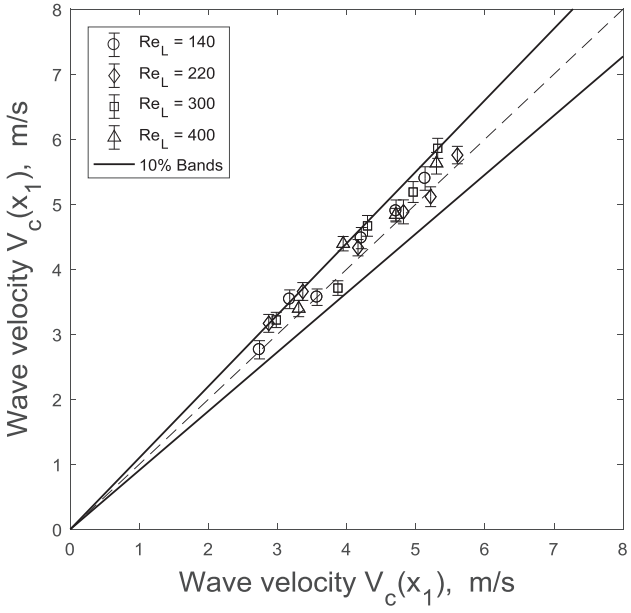

Fig. 5. Evolution disturbance wave speed between $x_1 = 330$ mm and $x_2 = 430$ mm for the upwards configuration. The error bars displayed were obtained by measuring the root-mean-square error of the linear approximation for each data point. V_G varies between 22 and 57 m/s.

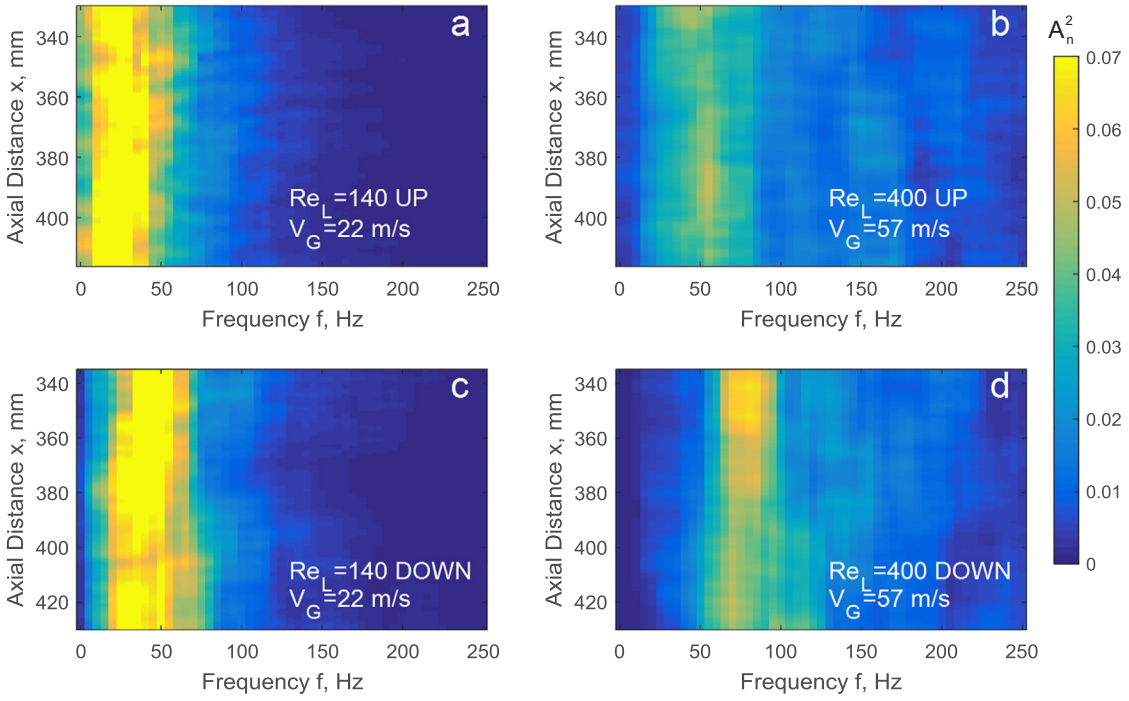

Fig. 6. Evolution of the temporal spectrum of film thickness records with downstream distance for upwards flow (a, b) and downward flow (c, d).

spatiotemporal plots, such constraints can be overcome, by allowing to automatically identify the spatiotemporal location of each individual wave. This poses an advancement on the statistics in comparison with previous studies of individual waves, as not only mean values but also the distributions of the measured parameters can be obtained, which allows for an enhanced validation of CFD models.

3.3.1. Description of tracking algorithm

In order to do so, a tracking algorithm based on the principles developed by Alekseenko et al. [31] was constructed and applied to the spatiotemporal plots recorded. In order to implement it, several steps had to be taken. First, the film thickness time series for the first pixel in the x coordinate of a given spatiotemporal plot was taken. It is possible to compute the peaks present in the data, as shown in Fig. 7(a).

It can be seen from Fig. 7(a) that not only the peaks corresponding to the disturbance waves were detected, but also the peaks related to the ripple waves present in the base film. In order to differentiate between both, a thresholding to the film thickness was applied, which was chosen to be 2.5 times higher than the median film thickness. Furthermore, detected peaks that were located within 50–100 points (depending on the flow regime) were taken as a single wave (Fig. 7b). Now that the initial position of each disturbance wave in the spatiotemporal plot is known, it is required for its full trajectory to be found. This is done based on the knowledge of the average wave velocity, V_c, which can be measured through the *indirect method* described in the previous section. By knowing the initial position of the wave and its velocity, it is possible then to predict its location after for instance, 50 pixels in the axial location. This assumes however, that all the disturbance waves are travelling at a speed equal to the average speed measured using the cross correlation, which is not true as their individual velocities vary around this mean value. In order to take this into consideration, computation on the location of which individual wave after 50 pixels is done with their individual velocity, V_{DW}, ranging between $0.6 < V_{DW}/V_c < 1.4$. From all the trajectories measured for each

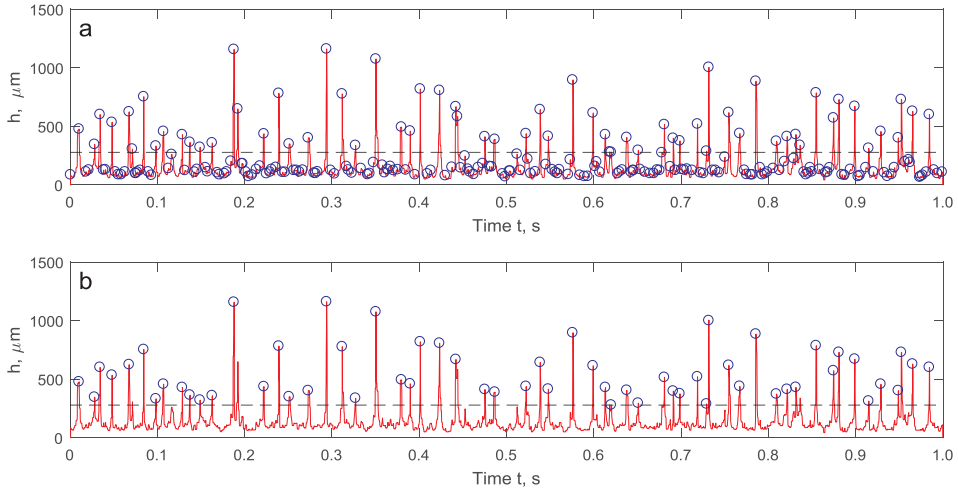

Fig. 7. (a) Temporal record of film thickness at $x = 330$ mm for the case of $Re_L = 140$ and $V_G = 57$ m/s in upward flow, with the local maxima of film thickness marked with circles. (b) Selection of local maxima corresponding to the disturbance waves using the film thickness threshold (dotted line).

individual wave, the point with the highest value of film thickness was chosen, as it is the one correspondent to the true disturbance wave trajectory. This was done for each individual wave, for every 50 pixels interval until the end of a given spatiotemporal plot. Finally, a best fit line is plotted for the trajectory of each wave based on the detected wave location at every 50 pixels. An example of the result of the application of such procedure is seen in Fig. 8. In this figure, the trajectories are shown only for the waves fully observed in the presented fragment.

3.3.2. Velocity estimation using tracking algorithm and comparison with indirect method

To measure the average disturbance wave velocity, $\langle V_{DW} \rangle$, using the tracking algorithm, the average slope of all the trajectories of disturbance waves relative to the *t*-axis for each regime point was calculated. As seen in Fig. 9, there is a close agreement between both *direct* and *indirect methods* used to measure the disturbance wave velocity.

The uncertainty associated with the *direct method* of measuring the average disturbance velocity is dependent on the success of the applicability of the tracking algorithm, which can be affected by a false positive (i.e. an identified wave that is not actually a disturbance wave) or false negative detections. The performance of the tracking algorithm was attested by visually checking the identified trajectory of each disturbance wave for all the regime points studied and no false positive was identified. As a result, the uncertainty associated with the *direct measurement* of the average disturbance wave velocity was measured by taking into consideration the standard deviation σ, on the individual velocities of the identified waves and also on N, the number of readings taken (i.e., the number of waves identified). This can be quantified using a quantity called standard error of the mean, which is estimated using the following relationship:

$$s_m = \frac{\sigma}{\sqrt{N-1}} \tag{8}$$

It is such that the mean value of a given sample has a 95% chance of lying within $\pm 2s_m$ of the true value. Therefore, $2s_m$, is a measure of how close to the mean value of a given parameter is to its unknown true value. The application of such approach to estimate the uncertainty of the *direct* disturbance wave velocity can be seen in the form of error bars in Section 3.4.

3.3.3. Frequency estimation using tracking algorithm and comparison with indirect method

In order to *directly* measure the frequency of disturbance waves, the number of waves detected by the tracking algorithm was simply counted and divided by the time of capture.

Unlike the case of the previous parameter, where close agreement is observed between the performance of the *direct* and *indirect* methods, this is not the case in terms of the disturbance wave frequency. Fig. 10 shows that the deviation in the measured parameter can surpass the 30% bands. This can be attributed mostly to the high level of uncertainty associated with the application of the FFT function, as detailed in Section 3.2.3 and to the lack of effectiveness of this procedure when dealing with non-periodical data.

As reported by Huang et al. [38], for a successful application of FFT method, the system must be linear and the data must be strictly periodic or stationary, otherwise the resultant spectrum can make little physical sense. Due to the non-periodicity associated with the disturbance wave behaviour, in subsequent references to the disturbance wave frequency, the values quoted refer to the values obtained through the *direct method*. The uncertainty of the tracking algorithm relates to the number of disturbance waves that were missed by the algorithm, whose as discussed previously, its performance was manually inspected. Although unlikely, the chance of missing waves was higher in the high gas superficial velocity cases, where the frequency of the disturbance waves was high, and the flow was much more irregular. More specifically, in some instances, disturbance waves were missed because their local amplitude was below the film thickness threshold set at the first pixel in the coordinate, as shown in Fig. 7. Consequently, it was estimated that in these high gas superficial velocity cases, that there is a 5%

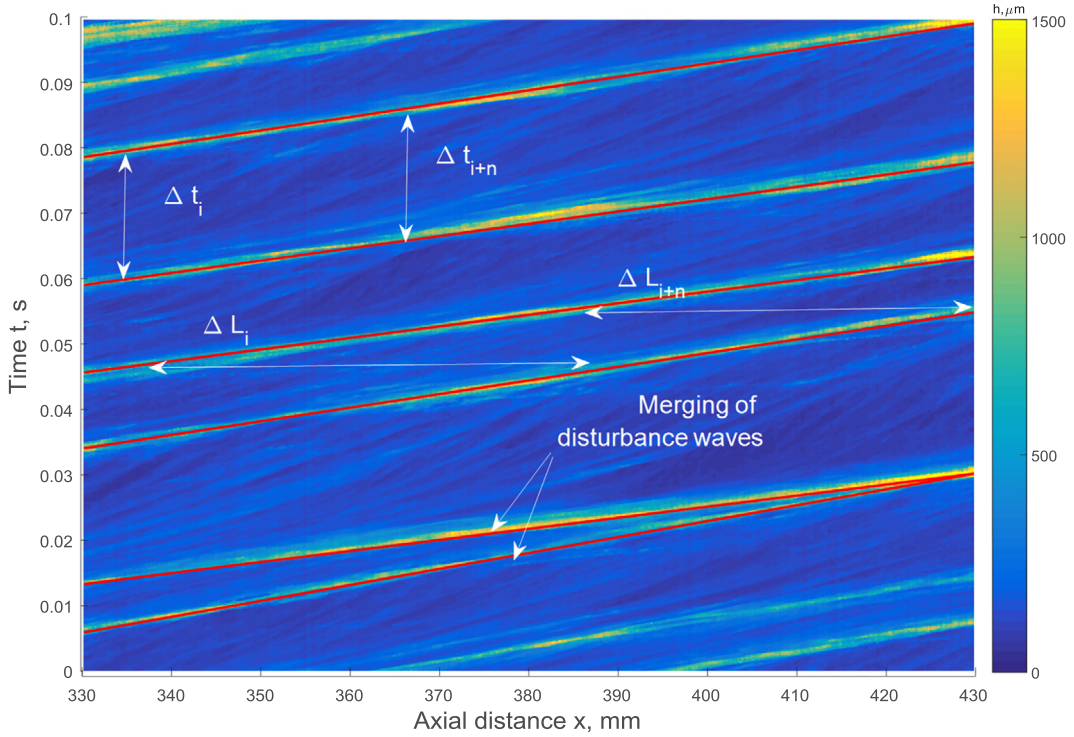

Fig. 8. Example of the application of the tracking algorithm at $Re_L = 400$ and $V_G = 43$ m/s in the downwards configuration. The detected trajectories of disturbance waves (red lines) are superimposed onto the spatiotemporal record of film thickness. (For interpretation of the references to colour in this figure legend, the reader is referred to the web version of this article.)

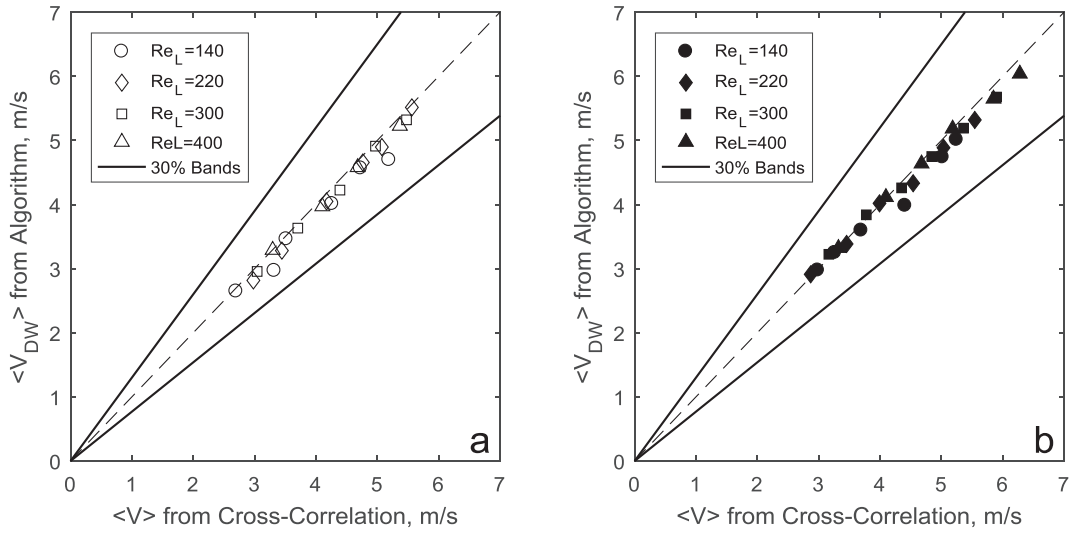

Fig. 9. Comparison of the performance of direct vs indirect methods in the measurement of disturbance wave velocity for (a) upwards and (b) downwards flows. V_G varies between 22 and 57 m/s.

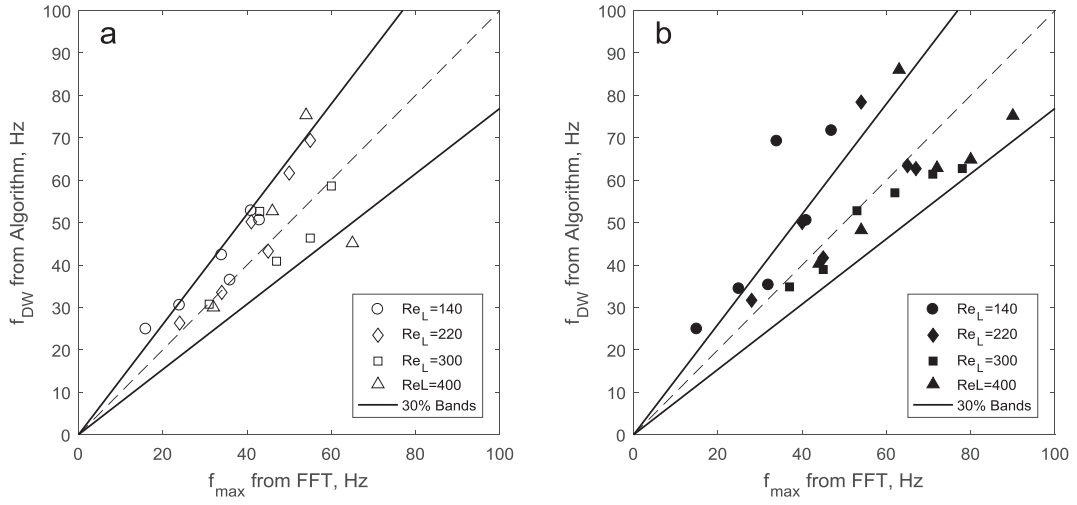

Fig. 10. Comparison of the performance of direct vs indirect methods in the measurement of disturbance wave frequency for (a) upwards and (b) downwards flows. V_G varies between 22 and 57 m/s.

underestimation on the total waves detected, and this uncertainty is shown in the form of error bars in Section 3.4, where a direct comparison of the flow orientation on the disturbance wave frequency is established.

3.3.4. Average time and distance separation between disturbance waves and comparison with indirect method

In the measurement of the average time separation, $\langle T \rangle$, between disturbance waves, the time difference $(t_1 - t_2)$, between consecutive waves was measured for every 50 pixels in the longitudinal axis, as shown diagrammatically in Fig. 8, and then a mean of these values was calculated. This provides an overall mean of the time separation between all consecutive pairs of waves. For the spacing between disturbance waves, the following approach was taken. Consider a consecutive pair of disturbance waves that is characterised by the time, t_1 and t_2, at which they reach a particular downstream position, x, and by their velocities at this point, V_1 and V_2, for each wave respectively. The wave spacing can be defined as the difference between their x-coordinate at the time moment $t = (t_1 + t_2)/2$. To obtain the average wave spacing, $\langle L \rangle$, this distance was measured using the following formula for each wave pair, from which the average was taken:

$$L = \frac{(V_1 + V_2)(t_2 - t_1)}{2} \tag{9}$$

The uncertainty associated with the estimation of average time separation and spacing of disturbance waves was measured using Eq. (8) to calculate the standard error of the mean within 95% confidence, $2s_m$. Here, σ, is the standard deviation of the individual separations obtained for each consecutive disturbance wave pair, and $N = f_{DW} - 1$. The result of the application of this methodology is shown in Fig. 11. Additionally, a comparison between the measured average time and wave spacing results and classical *semi-direct methods* of estimating these parameters is shown. More specifically, the latter consists on the time separation estimation using $1/f_{DW}$ and on the wave spacing estimation using the ratio of $\langle V_{DW} \rangle / f_{DW}$.

It can be seen that the magnitude of the error bars decreases in general with gas superficial velocity. This can be attributed to the fact that the frequency of disturbance waves is also increasing with this parameter, and consequently the variation of both the time separation and wave spacing is reduced. Despite the relatively high uncertainty of the measurement, there is generally a close agreement between both the *direct* and *semi-direct methods* used to measure these parameters. There are however, 5 instances in the wave spacing parameter where

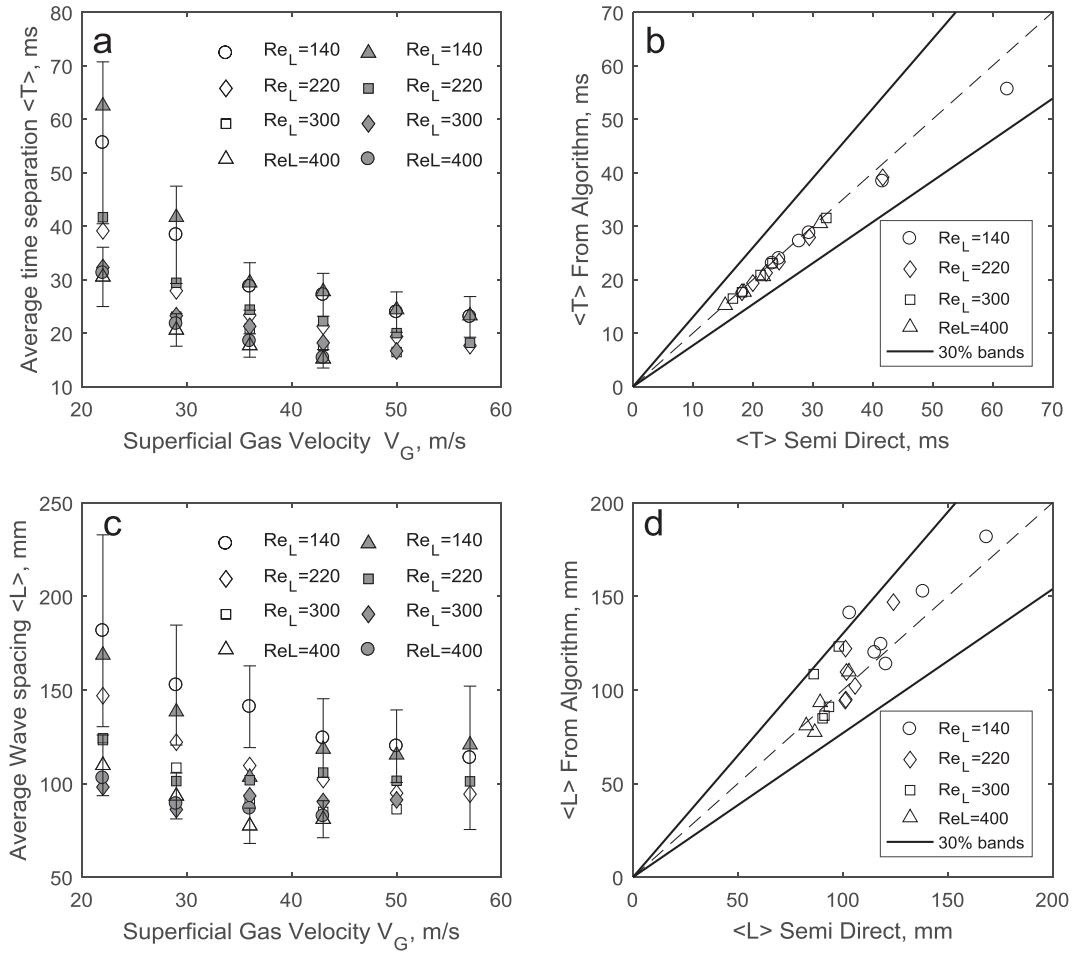

Fig. 11. Time separation (a and b) and wave spacing (c and d) measured using direct (algorithm) and semi-indirect methods for upwards flow. Similar trends were observed for the downwards case. For easiness of observation, error bars were only plotted for the cases of $Re_L = 140$ and $Re_L = 400$. Filled symbols in (a and c) denote the Semi-direct method, open symbols denote calculation from algorithm.

there is a deviation from the agreement. This disagreement can be attributed to the high sensitivity of the semi-indirect method, which is dependant on two variables (velocity and frequency). As shall be seen in Section 3.4, in some instances, the values of both velocity and frequency are slightly deviated from the increasing linear trend expected to be seen with increasing gas flowrate, which affects the semi-indirect results. Nonetheless, the general close agreement, substantiates the validity of the application of this direct method.

3.3.5. *Disturbance wave intermittency*

As discussed in Section 3.1, one of the initial stages that are behind the implementation of the tracking algorithm is the automated detection of the location of the peaks of each disturbance wave, as denoted by the orange point in Fig. 12. This principle was employed to compute the intermittency of the disturbance waves, or in other words, the total time that the disturbance waves are present in the signal over the total length of the time series record. By identifying the highest location of each disturbance wave, it was possible to find out the points where the

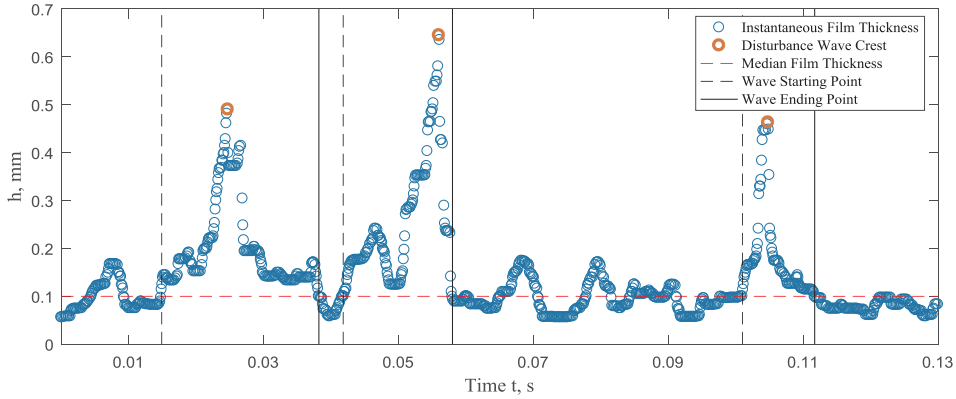

Fig. 12. Schematic of the implementation of the method to measure the intermittency of disturbance waves. This example shows a segment for $Re_L = 140$ and $V_G = 22$ m/s in upward flow.

disturbance wave starts and finishes and hence the length of time each wave takes to pass that particular measurement point.

This was achieved by computing the first point where the film thickness crosses the median film thickness level immediately before and after this peak point (as shown diagrammatically in Fig. 12, and then summing the total time spent by each individual disturbance wave in the time series. This was performed for all the spatiotemporal plots obtained for both upward and downward orientations. The total intermittency, *Int*, is a computation of the mean from the implementation of this technique over the entire longitudinal coordinate. The uncertainty of this procedure was quantified by calculating the standard mean error within 95% confidence level, $2s_m$, where, σ is the mean standard deviation of the intermittency results from all the points in the longitudinal coordinate ($N = 1024$ pixels). This will be shown in the form of error bars in Fig. 16 in Section 3.4.

With the best practices employed in the determination of disturbance wave parameters decided, the focus is now shifted towards the study of the effect of flow orientation on the behaviour of the annular flow regime. This is covered in the following sections.

3.4. The effect of flow orientation on film thickness and on disturbance waves

The interrelation between the liquid film flow rate per unit width, q, film thickness, h, and interfacial shear stress, τ_s, can be described by a solution of Navier-Stokes equations in integral form for a simplified case of unperturbed liquid film (see, e.g., Eqs. (4) and (9) in Alekseenko and Nakoryakov [39]):

$$q = \frac{\tau_s h^2}{2\mu}\left(1 \pm \frac{2\rho g h}{3\tau_s}\right) \tag{10}$$

Here ρ and μ are, respectively, liquid density and dynamic viscosity, and g is gravity acceleration. The positive sign of the last term corresponds to the case of downward flow and negative – to upwards flow. There are several straightforward consequences of this solution which are of importance for the subsequent analysis:

(1) For constant q, an increase in τ_s (which grows with gas velocity) leads to a decrease in film thickness, h. Consequently, this leads to an increase in the liquid velocity averaged across the depth of the film, $\langle V_L \rangle$, since $q = h\langle V_L \rangle$;
(2) For constant τ_s, increases in q causes an increase in both h and $\langle V_L \rangle$;
(3) For constant q and τ_s, the film will be thicker and slower in the case of the upwards flow;
(4) For larger film thicknesses, the difference between upwards and downwards configurations will be stronger;
(5) When $\rho g h \ll \tau_s$, the difference between the upwards and downwards cases will become negligible;

A comparison of the data on mean film thickness and thickness of the base film is presented in Fig. 13. Subfigures (a) and (b) show the dependence of the quantities on gas velocity for different liquid flow rates. Both quantities decrease with gas velocity and increase with liquid flow rate, in accordance with the anticipated behaviour (1) and

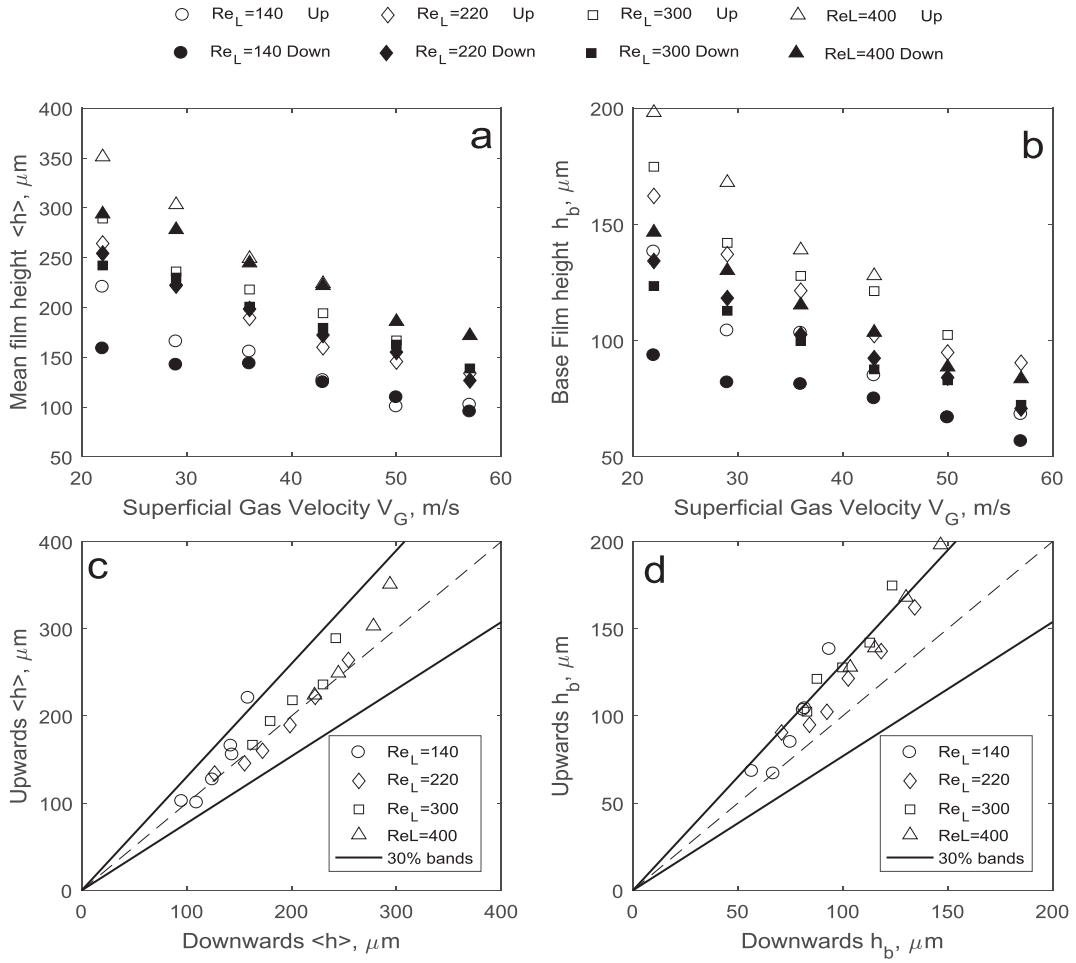

Fig. 13. Measured values of mean film thickness (a, c) and base film thickness (b, d). (a) and (b) refer to the dependence of these parameters on the gas velocity, whereas (c) and (d) display the direct comparison between upwards and downwards flows.

(2), respectively. Subfigures (c) and (d) show the direct comparison of measurements in upwards flow plotted versus the same measurements in downwards flow for the same conditions, along with border lines showing the difference of ± 30%. The mean film thickness is only affected by flow orientation at the lowest gas velocity, V_G = 22 m/s, as seen in Fig. 13c. At this velocity, the mean film thickness is larger for the upwards configuration, as it could be expected from the consequence (3). For higher values of V_G, the difference in the mean film thickness between upward and downward flows is negligible. One could assume that for the region $V_G > 22$ m/s, consequence (5) is true: the gravity effect becomes negligible and flow of liquid film (in both the base film and disturbance waves) is identical in the two cases.

However, comparison of the base film thickness (seen in Fig. 13d) demonstrates a much stronger difference between the two cases, which remains significant even for the highest gas velocities. Such a discrepancy denotes that the film properties are essentially different in the two cases and the agreement in average film thickness is rather a coincidence, appearing due to averaging over different areas of liquid film, namely, the base film and disturbance waves.

For the comparison conducted here, the liquid film flow rate can be considered to be the same in upward and downward configurations, since the flow rate of the dispersed phase nearly does not depend on the flow orientation [15]. The liquid flow rate can be therefore expressed as:

$$q = h\langle V_L \rangle = h_b \langle V_{L,b} \rangle (1 - Int) + h_{DW} \langle V_{L,DW} \rangle Int \quad (11)$$

Bearing in mind Eq. (11), several explanations for the same mean film thickness but different base film thickness can be proposed:

(I) The average film thickness in the disturbance waves zone is lesser in upwards flow. This explanation is unlikely to be true, since it contradicts consequences (3) and (4), but still cannot be discarded completely. This quantity is the most difficult to measure due to the optical distortions discussed in Section 2;
(II) The intermittency of the disturbance waves is lower in upwards flow. Intermittency may change due to the decrease in the average longitudinal size of disturbance waves, $\langle L_{DW} \rangle$, or due to an increase in disturbance wave spacing, $\langle L \rangle$ (see the Introduction for definitions and Section 3.3 for the method of measurements);
(III) The average velocity of liquid in the base film, $\langle V_{L,b} \rangle$, is lower in upwards flow, keeping the liquid flow rate in the base film constant. This quantity cannot be measured directly without proper Particle Image Velocimetry (PIV) measurements, which are extremely difficult to obtain in annular flows. Still, the general behaviour of $\langle V_{L,b} \rangle$ is expected to be related to the velocity of the slow ripple waves, V_{RW};
(IV) The velocity of the liquid in the disturbance waves, $\langle V_{L,DW} \rangle$, is lower in upwards flow, which reduces liquid transport by the

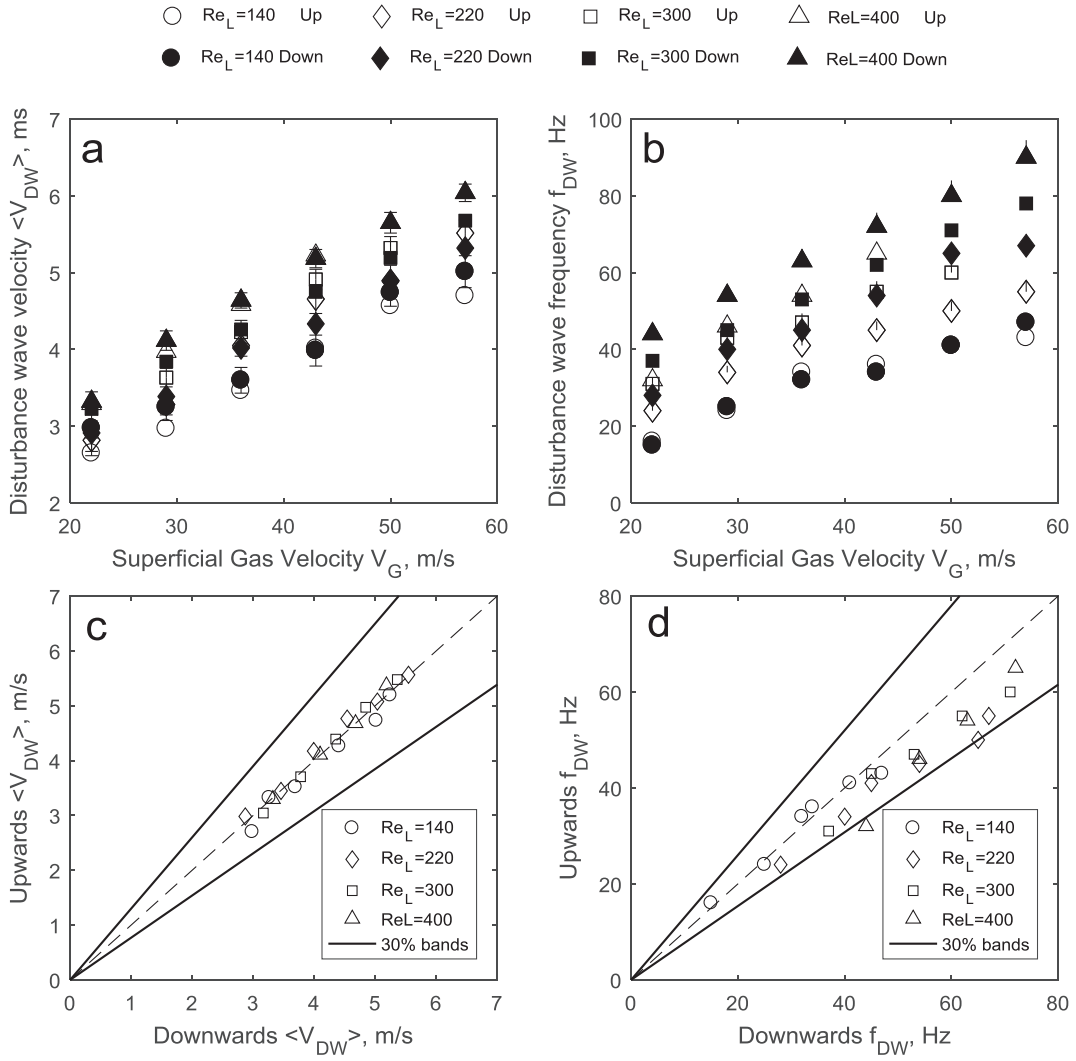

Fig. 14. Measured values of disturbance wave velocity (a, c) and frequency (b, d) with the tracking algorithm. (a) and (b) refer to the dependence of these parameters on the gas velocity, whereas (c) and (d) display the direct comparison between upwards and downwards flows.

disturbance waves. This velocity is expected to be quite close to the propagation velocity of the disturbance waves, V_{DW}.

Obviously, different explanations do not exclude each other and can act together. As a result, a direct comparison of the considered properties of disturbance waves is required. The properties were measured using the *direct measurement* approach, described in Section 3.3.

Fig. 14 shows the comparison of velocity (a, c) and frequency (b, d) of the disturbance waves. Both quantities show their usual behaviour: linear growth with gas velocity and weaker non-linear growth with liquid flow rate (as seen in Fig. 14a and b). It is interesting that the velocity of disturbance waves is approximately the same for different flow orientations (Fig. 14c). This agreement does not only allow us to discard the explanation (IV) listed above, but also helps to analyse the explanation (III). Indeed, the disturbance waves propagate over the base film, and its average velocity $\langle V_{L,b} \rangle$ is expected to contribute to the speed of the disturbance waves. Since the velocity of disturbance waves does not change with flow orientation, it can be assumed that the difference in the base film velocity, $\langle V_{L,b} \rangle$, is small enough in comparison to the velocity of the disturbance waves.

The independence of disturbance waves velocity on flow orientation does also remove a lot of ambiguity during the process of interpretation of the temporal records, e.g., during the comparison of disturbance waves frequencies (Fig. 14d). The passing frequency of the disturbance waves is seen to be higher in downwards flow. Since the velocities of disturbance waves are the same for both flow orientations, the difference in frequency denotes a difference in the disturbance waves spacing, $\langle L \rangle$, which is expected to be larger in the upwards flow. The spacing itself decreases with both gas and liquid flow rates (Fig. 15a). The direct comparison of this quantity (Fig. 15c) shows that the disturbance waves in the upwards configuration are separated by a larger distance, as anticipated in explanation (II).

The case of the smallest $Re_L = 140$ deviates from the other liquid flowrates, since it shows the same frequency and spacing for both flow orientations (Figs. 14d and 15c). On the other hand, it also shows a different behaviour in terms of longitudinal size of the disturbance waves, $\langle L_{DW} \rangle$, which is the other component of the intermittency, which can be measured with Eq. (1).

In general, $\langle L_{DW} \rangle$ decreases with gas velocity; for large liquid flow rates, it nearly does not depend on Re_L (Fig. 15b) and flow orientation (Fig. 15d). For $Re_L = 140$, $\langle L_{DW} \rangle$ shows much stronger dependence on gas flow rate (Fig. 15b) and it is definitely larger in downward flow (Fig. 15d).

The intermittency used in Eq. (11), increases with liquid flow rate and weakly decreases with gas velocity (Fig. 16a and b). For both flow orientations its values are definitely larger than those predicted by correlation of Schubring et al. [29]:

$$INT = 0.1 + \frac{Re_L}{40{,}000} \tag{12}$$

The difference may be attributed to a larger pipe diameter and the distance from the inlet in the experiments of Schubring et al. [29]: the disturbance wave frequency is known to be lower in large diameter

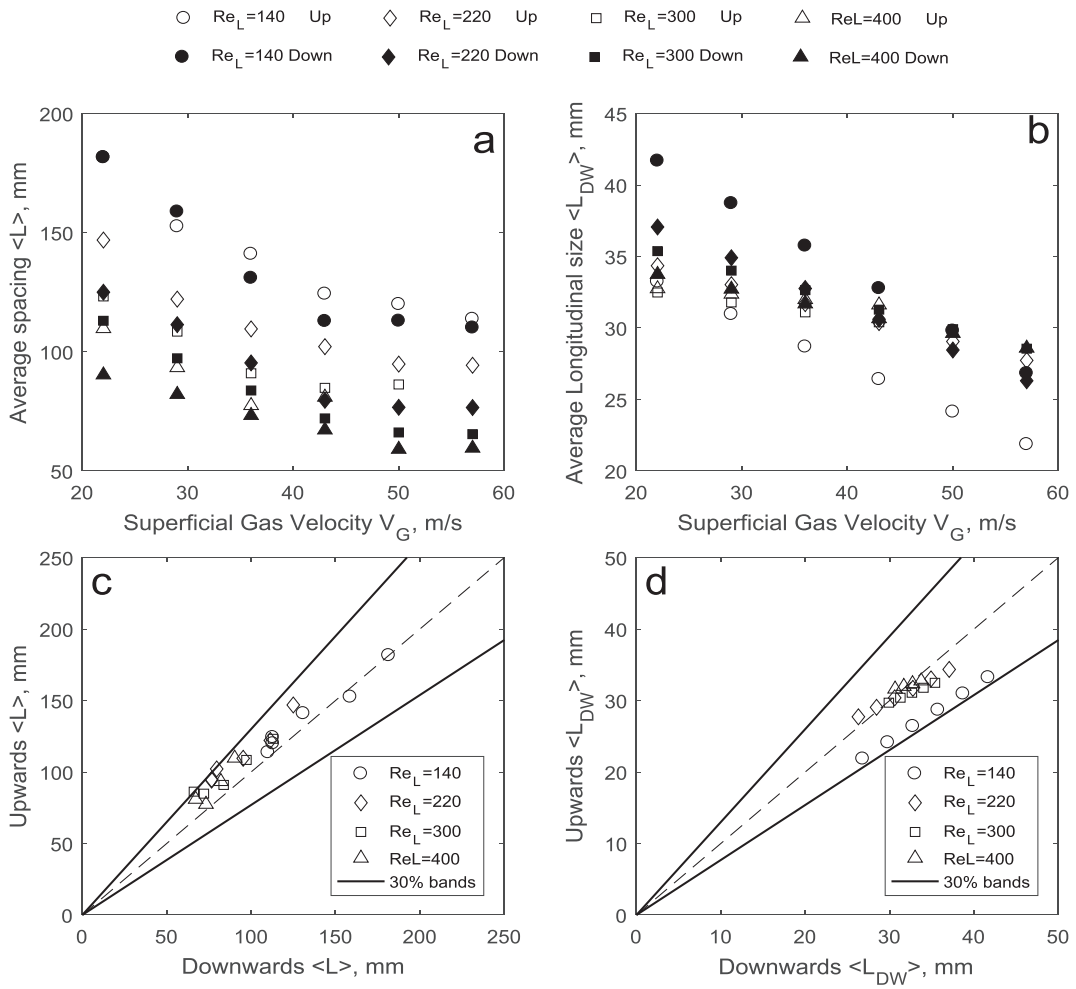

Fig. 15. Average spacing (a) and longitudinal size (b) of disturbance waves; direct spacing (c) and size (d) comparison for both flow orientations. The solid and hollow symbols in a) and b) correspond to the downwards and upwards flows, respectively.

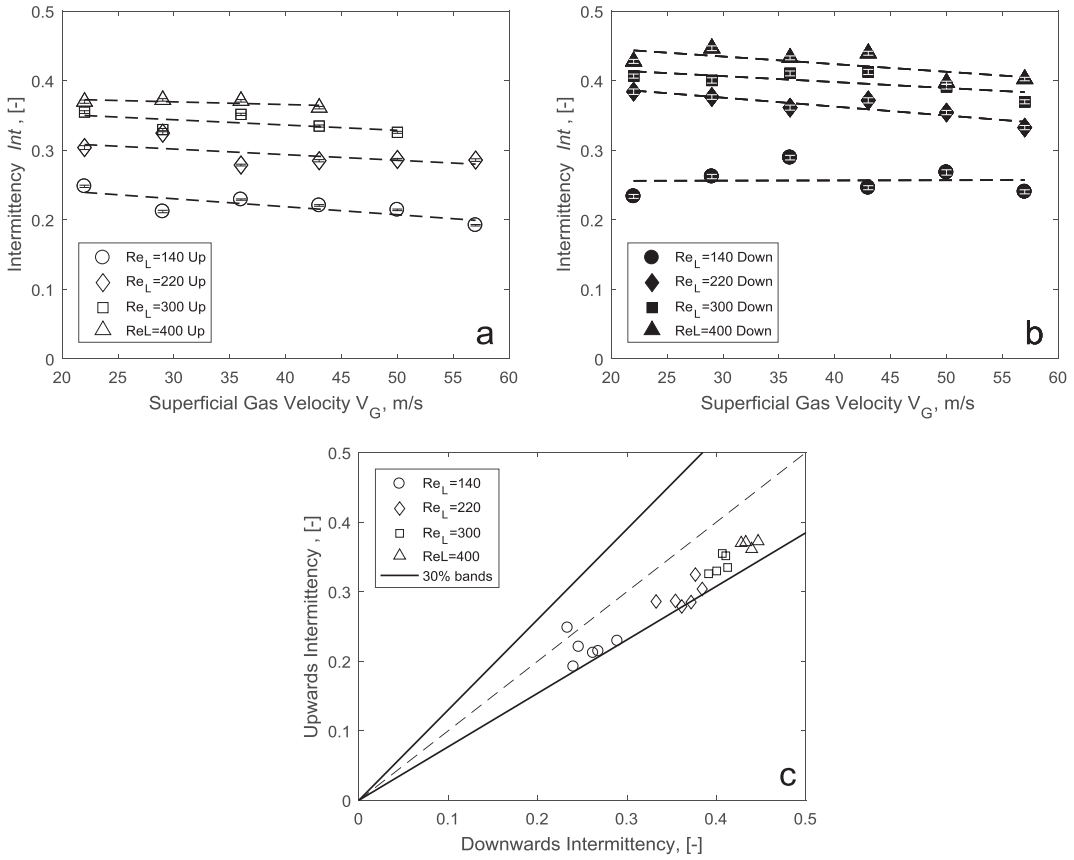

Fig. 16. Disturbance wave intermittency for (a) upwards and (b) downwards flows; (c) Direct comparison of the intermittency for both flow orientations.

pipes, and it also decreases with downstream distance. The main difference however is most likely to be related to the different method of determination of the disturbance waves. Schubring et al. [29] defined it by the threshold of illumination of the light passing through a disturbance wave: the light intensity will be strongly dampened, and this dampening occurs most strongly at the highly-perturbed surface of the crests of disturbance waves, which is covered with fast ripples. The length of this part of a disturbance wave is noticeably shorter than its full longitudinal size (see Fig. 18 in Alekseenko et al. [31]).

In this study, a comparison of the values of intermittency at different flow orientations using the same definitions is established. The intermittency is obviously larger in downwards flow (Fig. 16c). Interestingly, despite the fact that the cases of small and large liquid flowrates demonstrate different wave structures in terms of spacing and size of the disturbance waves, the effect of flow orientation on the intermittency is the same for all liquid flow rates.

To summarise, the thicker base film in upwards flow is at least partially compensated by the decrease in the disturbance wave intermittency, as suggested by explanation (II) above. This decrease occurs in a different manner for large and low liquid flow rates, either due to increase of disturbance waves spacing or due to decrease in longitudinal size of the disturbance waves.

In the next section, an analysis on how the velocity of liquid in the base film changes with flow orientation is performed. This will be achieved based on the velocity of the ripples present in it.

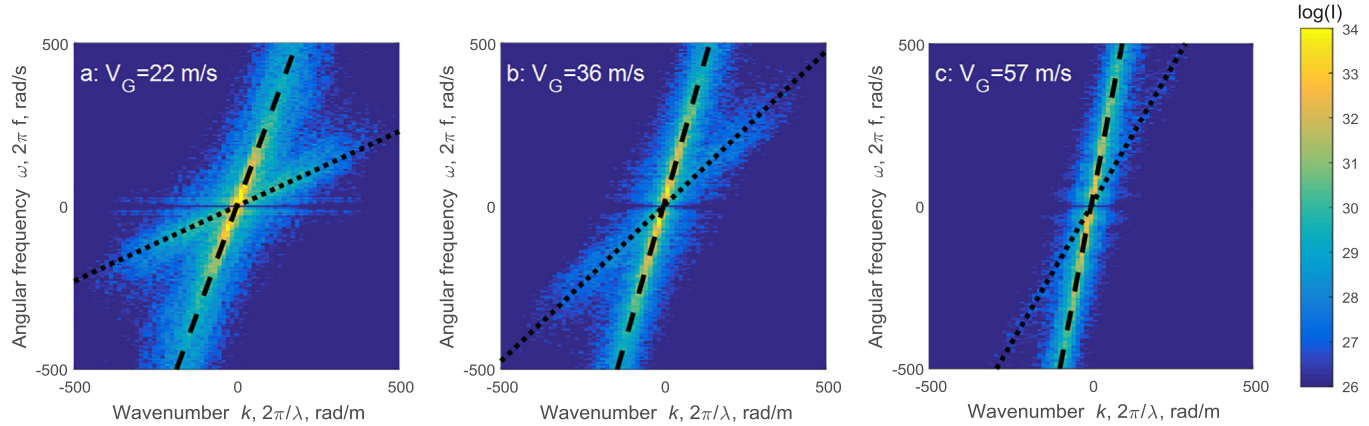

Fig. 17. Two dimensional spectra obtained by application of the $\omega-k$ analysis to spatiotemporal plots of film thickness for the case of $Re_L = 140$ for varying superficial gas velocity. The gradients of the dashed and dotted lines correspond to the velocity of the disturbance and ripple waves respectively.

3.5. Dynamics of slow ripples

Using spatiotemporally resolved data, it is possible to measure the velocity of the waves as ratio of their temporal frequency to spatial frequency. Alekseenko et al. [36] have shown this method to be in good agreement to other methods of measurements (see Fig. 9 in that paper). In the present work, this approach was developed into $\omega-k$ analysis. This analysis which may be referred to as 2D-FFT, consists in the simultaneous application of the Fast Fourier transform in both temporal and spatial domains. The result is shown in the form of plots of spectral amplitudes of angular frequency, ω, against that of the wave number, k, which is a function of the wavelength, λ, as shown for example in Fig. 17.

Fig. 17 shows that two bright lines were obtained from the analysis, highlighted by the best-fit lines. The lines correspond to the disturbance waves (brighter area) and the ripple waves (dimmer area), since they are the two predominant structures in the base film. The gradient of these lines corresponds to their average velocity, given by the following relationship:

$$c = \omega/k = f{\cdot}\lambda \tag{13}$$

The velocities obtained from the Omega-k analysis for the disturbance waves are in agreement with the velocities obtained from the application of both the *direct* and *indirect* methods detailed in Sections 3.2 and 3.3.

This resulted in the following trends shown in Fig. 18. This shows the resultant absolute mean velocities for both the disturbance and ripple waves. Increasing the gas superficial velocity leads to an increase in the velocity of the slow ripple waves, which travel at a much slower speed than that of the disturbance waves.

Following the argumentation of Alekseenko et al. [31], the data can be represented in the form of ratio of velocity of slow ripples to that of disturbance waves, as shown in Fig. 18b. For the downwards flow, the ratio is nearly independent of the gas velocity and liquid Reynolds number, which is in agreement to the results of Alekseenko et al. [31]. For the upwards flow, the ratio is also independent on liquid Reynolds number, but its dependence on the gas velocity is different. The ratio increases noticeably with gas velocity up to $V_G = 36$ m/s; at higher V_G, the increase in the velocity ratio still exists, but becomes much slower.

This complex behaviour is one of the observations which are not consistent with the straightforward application of the simplified smooth film force balance given in the beginning of Section 3.4. The other observations of this kind are:

(1) The disturbance waves are the areas of thicker film and they are anticipated to be more vulnerable to the effect of gravity than the base film. However, the properties of individual disturbance waves such as velocity have been shown not to be affected by the flow orientation (Fig. 14c), while the thickness of the much thinner base film layer is sensitive to flow orientation (Fig. 13d);
(2) The base film thickness, h_b, is of the same order of magnitude as mean thickness of thin gas-sheared liquid films in flow without liquid entrainment. The latter for the case of $Re_L = 40$ and $V_G = 36$ m/s was used as the reference value of film thickness, h_0, in BBLIF recalculations and was expected to be insensitive to flow orientation (see Section 2.2). Though the latter assumption was not validated directly, it is true that h_b has much stronger dependence on flow orientation than h_0. Indeed, even if the assumption on independence of h_0 on flow orientation was wrong and the real value of h_0 was higher in upwards flow, it would mean that the real value of h_b in upwards flow is even higher than it was measured by BBLIF.

One possible explanation for these inconsistencies is that the interfacial shear stress acting on the base film surface is much smaller than that acting on the surface of disturbance waves. It might even be smaller than that acting on the surface of thin gas-sheared films in absence of disturbance waves. This may be possible due to interaction of the gas stream with the disturbance waves, which act as large obstacles with a very rough surface due to presence of fast ripples. In the wake of these obstacles, the local gas velocity could possibly be significantly reduced. This assumption is supported by recent experiments by Buckley and Veron [40], who observed a strong decrease in longitudinal velocity of the gas phase in front of wind-driven waves in horizontal flow (see Figs. 4d and 7 in that paper). In such a case, the relative importance of gravity becomes much stronger for the base film between the disturbance waves.

Under this assumption, the qualitatively different behaviour of the slow ripple velocity in different flow orientations can be explained. In downward flow, all the liquid in both the disturbance waves and the base film flows downwards and the increase in gas velocity induces mostly quantitative changes in the dynamics of the waves. In upwards flow, the liquid inside the disturbance waves is definitely carried upwards by the strong gas shear, but the liquid present in the base film may at least partially flow downwards if the local gas shear is not high

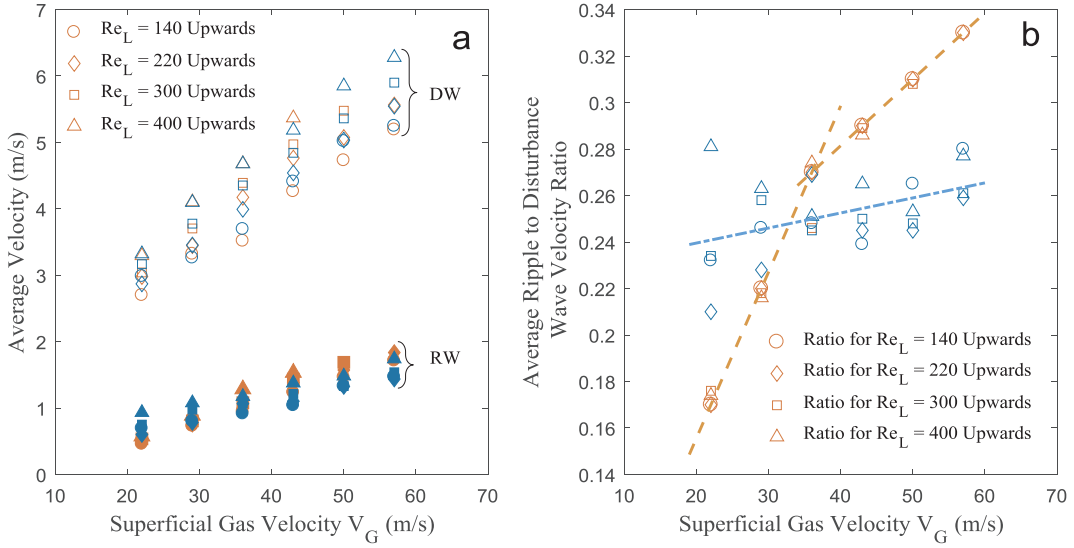

Fig. 18. (a) Absolute average disturbance (DW – open symbols) and ripple (RW-closed symbols) wave velocities for all cases; (b) Average ripple to disturbance wave velocity ratio. Orange and blue symbols refer to upwards and downwards cases respectively. (For interpretation of the references to colour in this figure legend, the reader is referred to the web version of this article.)

enough. Such intermittent direction of the liquid flow is well-known from studies of so-called “churn flow”, though this flow pattern is generally considered to occur at lower gas velocities than those used in our experiments. In such a case, at low and moderate gas velocities, only the near-interface layer of liquid with slow ripples may move upwards, against the bulk of liquid in the base film, which flows downwards. As a result, the ripples will be slowed down in comparison to the downwards flow. Such an idea is consistent with recent results obtained by Dasgupta et al. [22], who studied upwards flow in churn and annular flow patterns with high-speed imaging in an 11 mm pipe. They identified a transition between the two flow patterns at gas superficial velocities of 12–15 m/s. At lower gas velocities, the ripples on the base film moved downwards despite the already-upwards movement of disturbance waves and huge waves. In the transition region, the ripples on the base film were not moving neither upwards nor downwards. At higher gas velocities, the slow ripples moved upwards. It could be assumed that the final transition to fully upwards flow of all the liquid occurs around $V_G = 36$ m/s. Above this point, the effect of the gas velocity on the speed of the slow ripples will be approximately the same as in downwards flow, except for the fact that the still thicker base film will be responsible for a slightly higher velocity of the slow ripples in the upwards configuration.

4. Conclusions

In the present study, a direct comparison of disturbance waves and base film properties in upward and downward annular gas-liquid flows was conducted. The experiments were taken in adiabatic air-water flow with liquid entrainment at nearly atmospheric conditions in an 11.7 mm vertical pipe in the range of superficial gas velocities of 22–57 m/s and liquid Reynolds numbers of 140–400. The Brightness Based Laser Induced Fluorescence technique was used to acquire spatiotemporal records of local film thickness at axial distances that range between 330 and 430 mm (28–37 pipe diameters) from the inlet, where it was shown that the flow is close to a fully developed stage.

It was found that, despite the mean film thickness being only weakly affected by the flow orientation, the thickness of the base film between the disturbance waves is 10–30% higher in the upwards flow. This discrepancy may be explained by local decrease of the interfacial shear stress on the base film surface caused by the disturbance waves acting on the gas stream as large-scale rough obstacles, which leads to a decrease of gas velocity in the wake of the disturbance waves. This explanation is in agreement with the results of studying slow ripple waves on the base film using two-dimensional spectral analysis. Qualitatively, a different dependence of the velocity of slow ripples on superficial gas velocity was observed in upwards and downwards flow configurations. For the upwards flow, the suggested transition to the flow in which all liquid flows upwards, occurs at gas velocity around 36 m/s.

The properties of the disturbance waves were analysed using a tracking algorithm that automatically detects the spatiotemporal location of each disturbance wave (*direct method*). The algorithm was shown to be a more comprehensive tool for measuring disturbance wave frequency, spacing and intermittency in comparison to commonly used *indirect approaches*.

It was shown that the flow orientation has no noticeable effect on the velocity of the disturbance waves. The increased liquid flow rate in the base film in case of the upwards flow is compensated by a reduced disturbance wave intermittency. Moreover, in comparison to downwards flow, the intermittency may be reduced either due to a decrease in the longitudinal size of the disturbance waves (at low liquid Reynolds numbers), or due to an increase in the distance between the disturbance waves (at high liquid flowrates).

Acknowledgements

The experimental cycle with application of the BBLIF technique was conducted with the financial support of the Russian Science Foundation (project 16-19-10449). The work on data processing and analysis was funded by the Royal Society (project IE150086) and the Engineering and Physical Sciences Research Council (EPSRC), UK (project EP/K003976/1).

References

[1] K.J. Chu, A.E. Dukler, Statistical characteristics of thin, wavy films III. Structure of the large waves and their resistance to gas flow, AIChE J. 21 (1975) 583–593.
[2] N. Hall Taylor, G.F. Hewitt, P.M.C. Lacey, The motion and frequency of large disturbance waves in annular two-phase flow of air-water mixtures, Chem. Eng. Sci. 18 (1963) 537–552.
[3] N.S. Hall Taylor, R.M. Nedderman, The coalescence of disturbance waves in annular two phase flow, Chem. Eng. Sci. 23 (1968) 551–564.
[4] A. Wolf, S. Jayanti, G.F. Hewitt, Flow development in vertical annular flow, Chem. Eng. Sci. 56 (2001) 3221–3235.
[5] Y. Zhao, C.N. Markides, O.K. Matar, G.F. Hewitt, Disturbance wave development in two-phase gas–liquid upwards vertical annular flow, Int. J. Multiph. Flow 55 (2013) 111–129.
[6] S. Alekseenko, V. Antipin, A. Cherdantsev, S. Kharlamov, D. Markovich, Two-wave structure of liquid film and wave interrelation in annular gas-liquid flow with and without entrainment, Phys. Fluids 21 (2009).
[7] I. Zadrazil, C.N. Markides, An experimental characterization of liquid films in downwards co-current gas-liquid annular flow by particle image and tracking velocimetry, Int. J. Multiph. Flow 67 (2014) 42–53.
[8] T. Hazuku, T. Takamasa, Y. Matsumoto, Experimental study on axial development of liquid film in vertical upward annular two-phase flow, Int. J. Multiph. Flow 34 (2008) 111–127.
[9] G.F. Hewitt, N.S. Hall-Taylor, Annular Two-phase Flow, first ed., Pergamon Press, Oxford, New York, 1970.
[10] S.M. Bhagwat, A.J. Ghajar, Similarities and differences in the flow patterns and void fraction in vertical upward and downward two phase flow, Exp. Therm Fluid Sci. 39 (2012) 213–227.
[11] Y. Jiang, K.S. Rezkallah, A study on void fraction in vertical co-current upward and downward two-phase gas-liquid flow-I: Experimental results, Chem. Eng. Comm 126 (1993) 221–243.
[12] J.Y. Lee, M. Ishii, N.S. Kim, Instantaneous and objective flow regime identification method for the vertical upward and downward co-current two-phase flow, Int. J. Heat Mass Transf. 51 (2008) 3442–3459.
[13] T. Oshinowo, M.E. Charles, Vertical two-phase flow: Part II. Holdup and pressure drop, Can. J. Chem. Eng. 52 (1974) 438–448.
[14] M. Ishii, M.A. Grolmes, Inception criteria for droplet entrainment in two-phase concurrent film flow, AIChE J. 21 (1975) 308–318.
[15] G.B. Wallis, The onset of droplet entrainment in annular gas–liquid flow, General electric report no. 62 GL127, 1962.
[16] J.R. Barbosa Jr, G.F. Hewitt, G. König, S.M. Richardson, Liquid entrainment, droplet concentration and pressure gradient at the onset of annular flow in a vertical pipe, Int. J. Multiph. Flow 28 (2002) 943–961.
[17] G.A. Hughmark, Heat transfer with phase change in vertical upward, horizontal, and vertical downward tube flow, Ind. Eng. Chem. Fundam. 21 (1982) 339–343.
[18] V.A. Antipin, L.I. Zaichik, Y.A. Zeigarnik, D.M. Markovich, S.L. Solov'ev, O.G. Stonik, S.M. Kharlamov, A.V. Cherdantsev, The development of a three-fluid model of two-phase flow for dispersed-annular mode of flow in channels: film thickness and pressure drop, High Temp. 41 (2003) 399–403.
[19] S. Anupriya, S. Jayanti, Studies of downward gas-liquid annular flow, in: 9th International Conference on Multiphase Flow, Florence, Italy, 2016.
[20] B.J. Azzopardi, Disturbance wave frequencies, velocities and spacing in vertical annular two-phase flow, Nucl. Eng. Des. 92 (1986) 121–133.
[21] R.J. Belt, J.M.C. Van't Westende, H.M. Prasser, L.M. Portela, Time and spatially resolved measurements of interfacial waves in vertical annular flow, Int. J. Multiph. Flow 36 (2010) 570–587.
[22] A. Dasgupta, D.K. Chandraker, S. Kshirasagar, B.R. Reddy, R. Rajalakshmi, A.K. Nayak, S.P. Walker, P.K. Vijayan, G.F. Hewitt, Experimental investigation on dominant waves in upward air-water two-phase flow in churn and annular regime, Exp. Therm Fluid Sci. 81 (2017) 147–163.
[23] H. Han, Z. Zhu, K. Gabriel, A study on the effect of gas flow rate on the wave characteristics in two-phase gas-liquid annular flow, Nucl. Eng. Des. 236 (2006) 2580–2588.
[24] R. Kumar, M. Gottmann, K.R. Sridhar, Film Thickness and wave velocity measurements in a vertical duct, J. Fluids Eng. 124 (2002) 634–642.
[25] R.M. Nedderman, C.J. Shearer, The motion and frequency of large disturbance waves in annular two-phase flow of air-water mixtures, Chem. Eng. Sci. 18 (1963) 661–670.
[26] K. Ohba, K. Nagae, Characteristics and behavior of the interfacial wave on the liquid film in a vertically upward air-water two-phase annular flow, Nucl. Eng. Des. 141 (1993) 17–25.
[27] P. Sawant, M. Ishii, T. Hazuku, T. Takamasa, M. Mori, Properties of disturbance waves in vertical annular two-phase flow, Nucl. Eng. Des. 238 (2008) 3528–3541.
[28] D. Schubring, T.A. Shedd, E.T. Hurlburt, Planar laser-induced fluorescence (PLIF) measurements of liquid film thickness in annular flow. Part II: Analysis and comparison to models, Int. J. Multiph. Flow 36 (2010) 825–835.
[29] D. Schubring, T.A. Shedd, E.T. Hurlburt, Studying disturbance waves in vertical

annular flow with high-speed video, Int. J. Multiph. Flow 36 (2010) 385–396.
[30] T. Tomida, T. Okazaki, Statistical character of large disturbance waves in upward two-phase flow of air-water mixtures, J. Chem. Eng. Jpn. 7 (1974) 329–333.
[31] S.V. Alekseenko, A.V. Cherdantsev, O.M. Heinz, S.M. Kharlamov, D.M. Markovich, Analysis of spatial and temporal evolution of disturbance waves and ripples in annular gas-liquid flow, Int. J. Multiph. Flow 67 (2014) 122–134.
[32] S.A. Schadel, T.J. Hanratty, Interpretation of atomization rates of the liquid film in gas-liquid annular flow, Int. J. Multiph. Flow 15 (1989) 893–900.
[33] G.R. Thwaites, N.N. Kulov, R.M. Nedderman, Liquid film properties in two-phase annular flow, Chem. Eng. Sci. 31 (1976) 481–486.
[34] D.R. Webb, G.F. Hewitt, Downwards co-current annular flow, Int. J. Multiph. Flow 2 (1975) 35–49.
[35] S. Alekseenko, A. Cherdantsev, M. Cherdantsev, S. Isaenkov, S. Kharlamov, D. Markovich, Application of a high-speed laser-induced fluorescence technique for studying the three-dimensional structure of annular gas-liquid flow, Exp. Fluids 53 (2012) 77–89.
[36] S. Alekseenko, A. Cherdantsev, O. Heinz, S. Kharlamov, D. Markovich, Analysis of spatial and temporal spectra of liquid film surface in annular gas-liquid flow, Exp. Fluids 54 (2013).
[37] P.D. Welch, The use of Fast Fourier Transform for the estimation of power spectra: a method based on time averaging over short, modified periodograms, IEEE Trans. Audio Electroacoust. AU-15 (1967) 70–73.
[38] N.E. Huang, Z. Shen, S.R. Long, M.C. Wu, H.H. Shih, Q. Zheng, N.-C. Yen, C.C. Tung, H.H. Liu, The empirical mode decomposition and the Hilbert spectrum for nonlinear and non-stationary time series analysis, vol. 454, in: Proceedings of the Royal Society of London, Series A: Mathematical, Physical and Engineering Sciences, pp. 903–995
[39] S.V. Alekseenko, V.E. Nakoryakov, Instability of a liquid film moving under the effect of gravity and gas flow, Int. J. Heat Mass Transf. 38 (1995) 2127–2134.
[40] M.P. Buckley, F. Veron, Airflow measurements at a wavy air–water interface using PIV and LIF, Exp. Fluids 58 (2017) 161.